

AD-A218 844

FINAL TECHNICAL REPORT

ONR Contract N00014-83-K-0365

"Solar Flares and Magnetospheric Particles:  
Investigations Based Upon the ONR-602 and ONR-604 Experiments"

John P. Wefel  
Principal Investigator

DTIC  
ELECTE  
MAR 8 1990  
S B D

Louisiana State University  
Department of Physics and Astronomy  
Baton Rouge, LA 70803-4001

14 February 1990

# **SOLAR FLARES and MAGNETOSPHERIC PARTICLES: INVESTIGATIONS BASED UPON THE ONR-602 AND ONR-604 EXPERIMENTS**

ONR Contract N00014-83-K-0365

John P. Wefel  
Principle Investigator  
Department of Physics and Astronomy  
Louisiana State University  
Baton Rouge, LA 70803-4001

## **I. INTRODUCTION**

Contract N00014-83-K-0365 was initiated after the successful flight of the ONR-602 experiment on the S81-1 pallet. The research involves both a technical/technological component and a scientific component, both aimed at a better understanding of the particle radiations encountered in the near-Earth (Geospace) environment.

The ONR-602 and ONR-604 instruments were conceived in the 1970's expressly for the purpose of studying the heavy ion component in Geospace. The instruments were designed and built at the University of Chicago, under the leadership of Professor John A. Simpson, assisted by scientists M. Munoz, G. Mason, K. Pyle, J. Wefel and R. Zamow and the engineering and technical staff of the Laboratory for Astrophysics and Space Research. The ONR-602 instrument, consisting of a main telescope and a smaller flux monitoring telescope, was designed to study the lowest energy flare and magnetospheric particles. The ONR-604 instrument was designed to extend the measurements to higher particle energies and to have sufficient collecting power to study the rarer species.

The ONR-602 experiment, named "Phoenix-1", was launched into a low-altitude polar orbit on the S81-1 Pallet mission and was active for seven months in 1982. This provided an opportunity to space test some of the new technology employed in the instruments, to reexamine the earth's low altitude magnetosphere during the 1982 epoch and to study low energy solar energetic particles. The ONR-604 instrument is to be launched into a highly elliptical (GTO) orbit in mid-1990 on the CRRES mission and will provide data complementary to that obtained from Phoenix-1. The CRRES program, scheduled for a 3-5 year mission duration, will provide unique data on both solar energetic particles and trapped radiations and will answer some of the remaining questions in the field.

Analysis of the data from the ONR-602 instrument has been conducted both by The University of Chicago and Louisiana State University, and a similar arrangement for joint work on the ONR-604 data from the CRRES mission has been formulated. For the ONR-602 analysis, LSU has responsibility for: (1) correlative studies on solar flares, involving

the collection of data from other spacecraft or ground-based observatories and the combination of this data with the ONR-602 results, and (2) magnetospheric particle investigations focusing on spatial and temporal variations and their relationship to solar flare/interplanetary conditions. Chicago has principal responsibility for first phase data processing and analysis of solar flare elemental and isotopic composition. For ONR-604, LSU will focus, initially, on the magnetospheric particles and on the correlative studies.

With the initiation of the CRRES mission for space radiation studies and the inclusion of ONR-604 as one of the major instruments on the mission, an additional opportunity for magnetospheric and solar flare science was established. As part of that program, the SPACERAD Science Team was formed to provide scientific planning in support of the overall mission objectives. LSU was asked by Prof. Simpson to join that science team both to represent and support the ONR-604 experiment and its vital role in the mission and to help incorporate the ONR-602 data into the overall picture of the magnetosphere which is expected to emerge from the CRRES/SPACERAD program. Thus, the work covered by this contract involved science analysis from the ONR-602 experiment coupled to science support/planning for the ONR-604 experiment, now scheduled to be launched in mid-1990 on an Atlas ELV.

## II. RATIONALE

The study of solar flares, and the interaction of solar flare radiations with the geospace environment, is one of the most fundamental investigations in space science. Involved are basic questions about the mechanism for energy generation in the flare region, the conversion of this energy into high energy charged particles, neutrons, x-rays and gamma rays, the interplanetary propagation of the particles to Earth, the access of these particles to the magnetosphere and the changes initiated in our local environment due to the solar flare. In the latter case, the solar particles are superposed upon an existing background of geomagnetically trapped and pseudo-trapped charged particles, which are themselves of fundamental importance in the dynamics of the geospace environment.

While these questions are quite compelling scientifically, they also have important practical applications. The influence of solar activity and the consequent geomagnetic disturbances on the availability and quality of long range, short wave radio communication is perhaps the best known of the solar effects. With the advent of the space program and the ever increasing use of the space environment for both civilian and military applications, the consequences of space radiations are a major operational concern since possible effects of such radiations include: the long-term degradation of hardware in the space environment, the abrupt failure of space systems due to a short-term event or even a single, intensely ionizing particle, and limitations imposed by the radiation environment on the human presence in orbit. Our ability to assess the resulting operational limitations depends both on detailed knowledge of the geospace environment and its spatial and temporal variability and on the degree of sophistication of the space systems that are required to operate there. As this sophistication increases, so does the need for more detailed knowledge of the environment and for development of a capability for predicting its characteristics over a given orbit.

The large fluences of protons and electrons encountered in Geospace combined with the solar ultraviolet flux are responsible for the degradation of exterior spacecraft components (e.g. solar panels) while induced potentials from the space environment can lead to major electrical discharges between different parts of a spacecraft (Mizera et al., 1980). For electronic components located within the spacecraft, the overall radiation dose can be large (depending upon the orbit), requiring spacecraft designers to employ radiation-hardened parts and, often, passive shielding which is costly in the form of increased weight.

There is, however, another source of radiation damage -- single particle induced effects -- which has been recognized as a major problem (Binder et al., 1975). There are two types of such single particle effects whose relative importance depends upon the character of the radiation environment and the type of electronic parts employed in a space system. First, protons or alpha particles can interact with the silicon substrate in an integrated circuit device and produce low velocity fragments that lose energy by ionization at a rate sufficient to interfere with the operation of the device (May and Woods, 1979; McNulty et al., 1980; Guenzer et al., 1980; Petersen, 1980). Fortunately, the interaction rate for protons and alphas is relatively small, but as the packing density of electronic circuits increases, these interactions may become a problem. Second, there is now ample evidence for a direct effect caused by heavy ions traversing integrated circuit devices, particularly low power memory chips (Kolasinski et al., 1979; Ziegler and Lanford, 1979; Hamm et al., 1979; Bruckner et al., 1980; Pickel and Blandford, 1980). Since the rate of ionization energy loss scales as the square of the particle's charge, the heavy ions deposit considerably more energy than protons and alphas, producing enough charge carriers within the sensitive region of the device to upset its logical state. Generically, such effects are called Single Event Upsets (SEU's).

Although the relative abundance of heavy ions is small compared to that of protons, the damage efficiency is high since the effects are caused directly by the passage of the particle through the device. In addition, the damage potential increases with the particle charge, making an energetic iron nucleus, for example, much more potentially damaging than an oxygen ion. The major concern for the future lies in the fact that as the sophistication level and device density of the electronic systems increases, the number of charge carriers involved per device decreases. This makes a device sensitive to effects caused by incident particles from a wider range of the charge spectrum and thereby increases the overall sensitivity of these systems to disruption by individual particles (see, for example, Iverson, 1979). The importance of this problem is such that a concerted effort is now underway to understand both the device sensitivity and the radiation environment in sufficient detail to aid in spacecraft design and operational planning. This is one of the main goals of the CRRES program.

The heavy ion component of the geospace particle environment is particularly important but has not been studied in sufficient detail. Adams et al. (1981) reviewed and summarized present knowledge of heavy charged particles in the galactic cosmic radiation, in solar flares (at varying levels of enhancement) and in the magnetosphere. The composition of the galactic cosmic rays is the best known, followed by that of solar energetic particles. The presence of heavy ions at relatively high energies in the magnetosphere remains a controversial question (see Adams and Partridge, 1982) requiring further study.

on ☒ ☐ ☐

*per Telian*

STATEMENT "A" per Dr. Michael Shlesinger  
 NRL/Code 1112  
 TELECON 3/7/90 VG

Distribution/Availability Codes	
Dist	Avail and/or Special
A-1	

Astrophysically, the heavy ion component is particularly important since the relative abundance of elements and isotopes in this component contains a characteristic "signature", which provides much of the information necessary to unravel the questions of the origin, acceleration and history of the particles. Thus, detailed investigation of the heavy ion component combines both scientific and practical goals and this is the motivation behind the ONR-602 and ONR-604 experiments and the investigations summarized here.

### III. DOCUMENTATION SUMMARY

The work performed under this grant has been discussed in a number of reports, presentations, published conference proceedings and journal articles. A chronological listing for this documentation is given below.

- (1) "Phoenix-1 (ONR-602) -- The Isotopes in Solar Flares," John P. Wefel, an invited talk presented to the STP Mission Review Meeting, Aerospace Corporation, Los Angeles, CA, August, 1983.
- (2) "Elemental and Isotopic Composition of Solar Energetic Particles: Preliminary Results from the Phoenix-1 Telescope," J. A. Simpson, J. P. Wefel and R. Zamow, Proceedings of the 18th International Cosmic Ray Conference (Bombay, India, 1983, Tata Institute of Fundamental Research), Vol. 10, p. 322.
- (3) "Annual Report: 4/1/83 - 3/31/84 for N00014-83-K-0365," submitted to the Office of Naval Research, 14 p.
- (4) "Galactic Cosmic Ray Isotopes and Elements: An Overview," John P. Wefel, an invited talk presented to the CRRES/SPACERAD Science Team Meeting, AFGL, Hanscom Air Force Base, October 1984.
- (5) "Investigations of Solar Charged Particles: The Phoenix-1 Experiment," T. Gregory Guzik, presented at the Workshop for a High Energy Facility for Solar Physics, University of New Hampshire, Durham, NH, October 1984.
- (6) "The Experiment for High Energy, Heavy Nuclei Composition (ONR-604)," J. A. Simpson, M. G. Munoz, M. Perkins and J. P. Wefel, in CRRES/SPACERAD Experiment Descriptions, eds. M. S. Gussenhoven, E. G. Mullen and R. C. Sagalyn, (Hanscomb AFB, MA; 1985; AFGL-TR-85-0017), pp. 163-173.
- (7) "Observations of 0.5 - 9 MeV Protons at Low Altitude in the Equatorial Radiation Belt during 1982," M. A. Miah, T. G. Guzik and J. P. Wefel, Bull. Am. Phys. Soc., 30, 778 (1985).

- (8) "Solar Flares and Magnetospheric Particles," John P. Wefel, presented at the Space Environment and Communications Workshop sponsored by ONR, University of Chicago, 16-17 May, 1985.
- (9) "Annual Report: 4/1/84 - 6/30/85 for N00014-83-K-0365," submitted to the Office of Naval Research, 14 p.
- (10) "Particle Precipitation at Low Altitudes near the Equator," M. A. Miah, T. G. Guzik and J. P. Wefel, Trans. Amer. Geophys. Union (EOS), Vol. 66, p. 1029 (1985).
- (11) "The Link Between Solar Energetic Particles and Gamma Ray Measurements," T. Gregory Guzik, presented to the Workshop on Gamma Ray Stars, Taos, NM, July 1986, .
- (12) "Annual Report: 5/1/85 - 6/30/86 for N00014-83-K-0365," submitted to the Office of Naval Research, 16 p.
- (13) "Observations of Low Energy Particle Precipitation at Low Altitudes in the Equatorial Zones," presented by M. A. Miah at the Third International School for Space Simulation, Beaulieu, France, June, 1987.
- (14) "Low Energy Protons at the Equator," presented by M. A. Miah at the Chapman Conference on Plasma Waves and Instabilities in Magnetospheres and at Comets, Sendai, Japan, October, 1987.
- (15) "Annual Report: Period ending 11/30/87 for N00014-83-K-1365," submitted to the Office of Naval Research, 22p.
- (16) "An Overview of Cosmic Ray Research: Composition, Acceleration and Propagation," John P. Wefel in Genesis and Propagation of Cosmic Rays, eds. M. M. Shapiro and J. P. Wefel (Dordrecht, Holland; 1988; D. Reidel Publ. Co.) pp. 1-40.
- (17) "The SEP Matter Sample and Its Correlation with Gamma Ray Observations," T. Gregory Guzik, Solar Physics, 118, 185-208 (1988).
- (18) "Phoenix-1 Observations of Equatorial Zone Particle Precipitation," M. A. Miah, T. G. Guzik, J. W. Mitchell and J. P. Wefel, in Genesis and Propagation of Cosmic Rays, eds. M. M. Shapiro and J. P. Wefel (Dordrecht, Holland; 1988; D. Reidel Publ. Co.) pp. 339-355.
- (19) "A Method for Mapping the Pitch Angles of Magnetospheric Particles onto a Detector Telescope: Detector Efficiency," presented by M. A. Miah at the Yosemite Conference on Outstanding Problems in Solar System Plasma Physics: Theory and Instrumentation, Yosemite National Park, CA, February, 1988.

- (20) "Nucleosynthesis, Nuclear Physics, Supernovae and Cosmic Rays," an invited paper presented to the 6th Course of the International School of Cosmic Ray Astrophysics, A NATO Advanced Study Institute, Erice, Italy, April, 1988.
- (21) "ONR-602 Results from 1982 Flares," presented by J. F. Cooper at the Second Workshop on Impulsive Solar Flares, Durham, NH, September, 1988.
- (22) "Annual Report: Period ending 11/30/88 for N00014-83-K-0365," submitted to the Office of Naval Research, 49p.
- (23) "Global Zones of Particle Precipitation," M. A. Miah, Ph.D. Dissertation, Louisiana State University, December, 1988.
- (24) "Altitude Dependence of Quasi-Trapped Protons in the Equatorial Zone," M. A. Miah, J. W. Mitchell, T. G. Guzik and J. P. Wefel, Trans. Amer. Geophys. Union, Suppl. List of Abstracts, p. 153 (1988).
- (25) "S81-1 Measurements of Low-Altitude Ions," J. P. Wefel, J. F. Cooper, T. G. Guzik and M. A. Miah, Trans. Amer. Geophys. Union (EOS), 69, 1389 (1988).
- (26) "Review of Pioneer-11 Data for High Energy Trapped Radiation in Saturn's Magnetosphere," W. Fillius, J. F. Cooper and R. B. McKibben, Trans. Amer. Geophys. Union (EOS), 69, 1398 (1988).
- (27) "Low-Altitude Trapped Protons at the Geomagnetic Equator," T. G. Guzik, M. A. Miah, J. W. Mitchell and J. P. Wefel, J. of Geophysical Research, 94, 145-150 (1989).
- (28) "Solar Flare Ion Measurements from the Polar Cap in 1982," J. F. Cooper, T. G. Guzik, J. W. Mitchell, J. J. Pitts and J. P. Wefel, Bull. Amer. Phys. Soc., 34, 1187 (1989).
- (29) "Magnetospheric Particle Detection Efficiency of a Conical Telescope," M. A. Miah, J. W. Mitchell and J. P. Wefel, Nucl. Instr. and Methods in Phys. Res., A281, 622-627 (1989).
- (30) "Energetic Particle Interactions with Planetary Material in the Saturn System," J. F. Cooper and J. P. Wefel, 21st ICR Conference Papers (Adelaide, Australia, 1990, University of Adelaide), Vol. 7, p. 260..
- (31) "Solar Flares in 1982 Measured from the Polar Caps," J. F. Cooper, T. G. Guzik, J. W. Mitchell, J. J. Pitts and J. P. Wefel, 21st ICR Conference Papers, (Adelaide, Australia, 1990, University of Adelaide), Vol. 5, p. 116.
- (32) "Final Technical Report for Contract N00014-83-K-0365," submitted to the Office of Naval Research (this report).

#### IV. INVENTIONS, PATENTS, COPYRIGHTS

There have been no inventions under this contract and no patents or copyrights have been granted or applied for.

#### V. SUMMARY OF RESEARCH RESULTS

The first phase of this project was initiated at LSU upon completion of data reduction at the Lockheed Palo Alto Research Laboratory (LPARL) and initial data processing at The University of Chicago. The ONR-602 counting rate dataset (CHART tapes) was transferred to LSU along with related software for magnetic field models and B, L coordinates. The initial analysis focused on magnetospheric particle studies, particularly in the equatorial regions, including a search for the signature of solar neutrons in the magnetosphere for the flare of June 3, 1982. Further progress required access to the full ONR-602 dataset. The University of Chicago finished its work on data processing/data quality checking and instrument response monitoring, and the full, uncompressed dataset (PHRET tapes), containing both pulse height and rate information, was transferred to LSU. At this time, our group became part of the VAX-11/750 based Experimental Physics Data System (EPDS), and the PHRET analysis software was developed on this system, which has the capabilities needed for the analysis of datasets such as ONR-602 and ONR-604. Scientific investigations have focused on solar energetic particles, correlative studies and magnetospheric particle populations, as well as preparation for the new ONR-604/CRRES data.

The analysis work performed under this contract can be divided into three areas: (i) Instrument response, (ii) Solar Energetic Particle investigations, and (iii) Magnetospheric particle populations. Our approach involved obtaining an overview of the entire ONR-602 dataset, finding and eliminating data processing/analysis/instrumental problems, identifying interesting effects for study, and investigating specific areas or problems of scientific/technical interest. A brief synopsis of results is presented below. More detail is contained in the documentation cited in Section III.

##### A. Instrumentation

Figure 1 shows schematic diagrams of the Low Energy Telescope (or Main telescope) and the Monitor telescope, the two instruments included as part of the ONR-602 package on the polar orbiting S81-1 Pallet mission, and the ONR-604 telescope for CRRES. A unique feature of the Main telescope and the ONR-604 High Energy Telescope is the inclusion of solid state position-sensing detectors (PSD's), shown in Figure 2, which were developed and fabricated at The University of Chicago (Lamport et al., 1976; 1980), and are used to determine the trajectory of each particle within the instrument. Such trajectory data allows the measurements in the other detectors to be corrected for the exact angle of incidence of the particle, and, combined with the spacecraft ephemeris, gives the arrival direction from space for each event. The ONR-602 experiment was the first use in the space environment of this new technology, and the PSD's performed well. By combining the particle trajectory measured by the PSD's with the energy deposited in the stack of solid state detectors, each particle triggering the



# INSTRUMENTATION

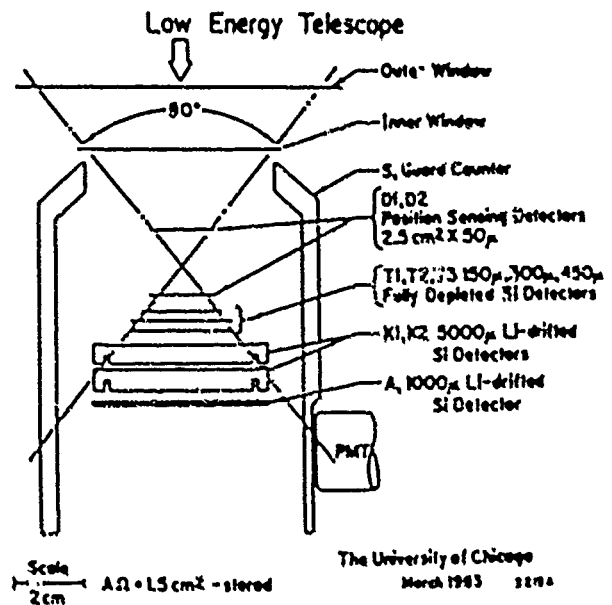
ONR - 602 ( on S 81-1 )

SEP ELEMENTS/ISOTOPES

Z: He - Ni

E:  $\sim 4 - 230$  MeV/N

GEOM:  $1.5 - 1.0$  cm<sup>2</sup>-SR



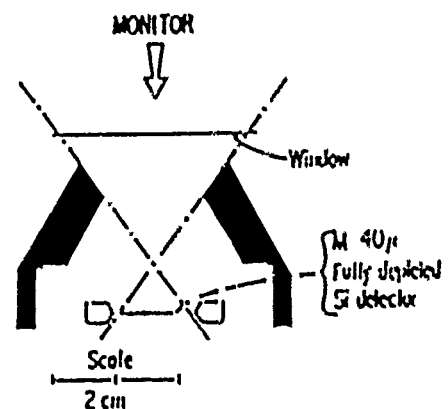
ONR - 602 ( on S 81-1 )

SEP & MAGNETOSPHERIC PARTICLE FLUX MONITORING

Z: p, He, Z > 2

E:  $\sim 0.6 - 10$  MeV/N

GEOM:  $0.5$  cm<sup>2</sup>-SR



ONR - 604 ( on CRRES )

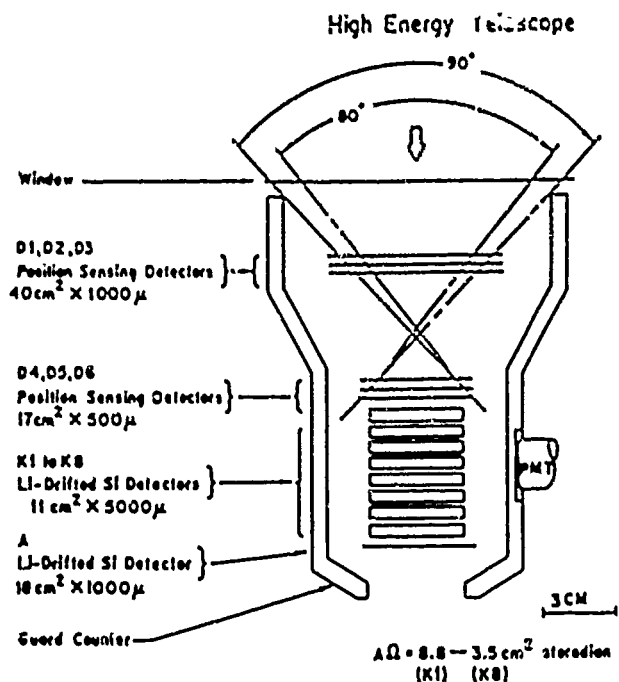
SEP & GCR ELEMENTS/ISOTOPES

MAGNETOSPHERIC HEAVY IONS

Z: H - Ni

E:  $\sim 25 - 570$  MeV/N

GEOM:  $8.8 - 3.5$  cm<sup>2</sup>-SR

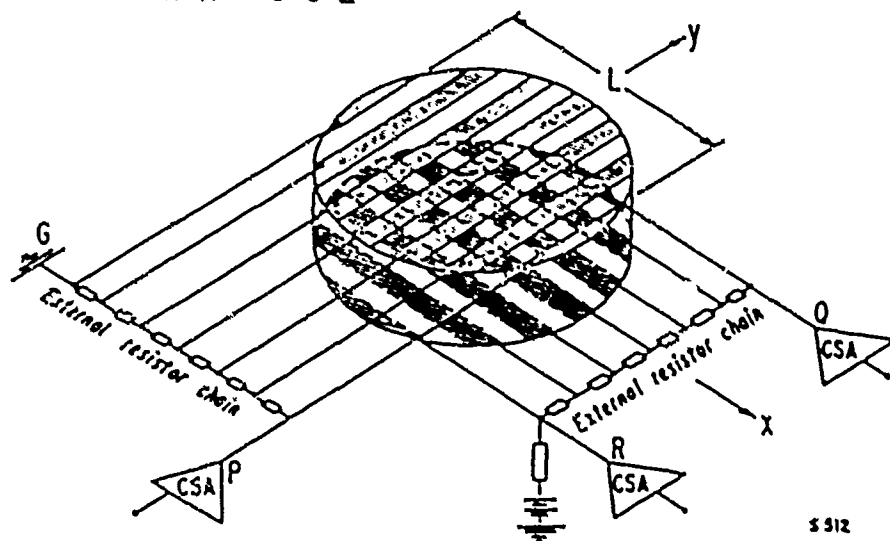


BUILT BY THE UNIVERSITY OF CHICAGO

Figure 1: Schematic Diagrams of the ONR Telescopes.

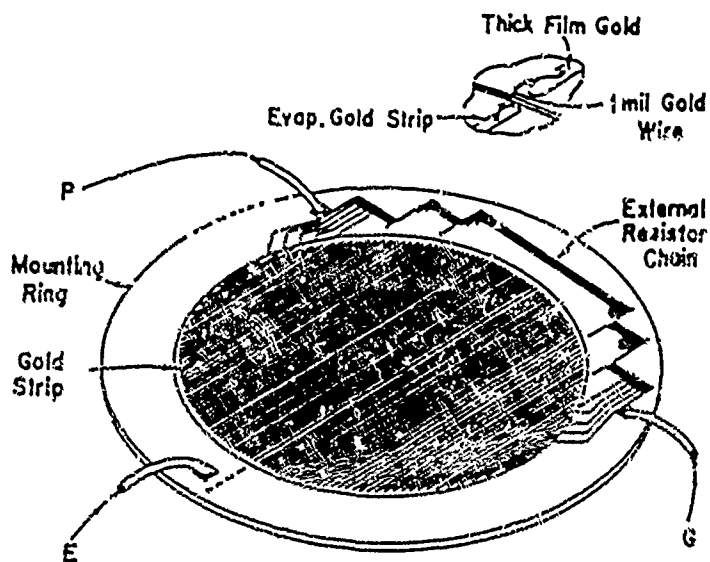
# SILICON DETECTOR TECHNOLOGY

ONR-602



The University of Chicago  
TWO-DIMENSIONAL POSITION SENSITIVE SILICON DETECTOR

ONR-604



The University of Chicago  
ONE-DIMENSIONAL POSITION SENSITIVE  
SILICON DETECTOR

S 762A

Figure 2: Position Sensing Detectors

event logic and coming to rest in the instrument has its charge, mass and energy measured. This allows the element distribution, the energy spectrum and the isotopic distribution of the recorded events to be studied in detail.

The Monitor telescope consists of a single, thin (40 micron thick) solid state detector surrounded by passive shielding, sufficient to absorb protons with energies up to about 40 MeV. There is no pulse height analysis for this telescope, but low energy particles are monitored by three counting rates, ML, MM and MH whose corresponding thresholds are adjusted so that they respond to  $Z \geq 1$ ,  $Z \geq 2$  and  $Z \geq 4$  particles, respectively. The thin detector and the selected thresholds make the Monitor insensitive to electrons. The Monitor rates are available for studying particles at energies, typically around 1 MeV/nucleon, below those needed to trigger the Main telescope.

The ONR-602 package was in nearly polar, 90 minute period, dawn-dusk orbit. The instruments, therefore, alternated between low counting rates near the equator and high counting rates in the polar regions. In addition, there were data gaps due to the power limitations imposed by the spacecraft. Consequently, it was necessary to spend considerable time trying to understand the instrument response to these varying environmental conditions and to obtain accurate calibrations of the thresholds, particle energy ranges, backgrounds for the measurements and available coverage.

The Challenger disaster delayed the launch of CRRES until mid-1990 and converted the program from a shuttle launch to an expendable launch vehicle. The initial launch will be to a Geosynchronous Transfer Orbit (GTO) with perigee of ~400 km, apogee ~6.6  $R_E$  and inclination  $< 28^\circ$ . (Chemical releases will take place during various parts of the CRRES mission and will be monitored by both CRRES instruments and other experiments.) This orbit will take CRRES through the heart of the inner (proton) and outer (electron) trapped radiation regions as well as providing measurements of interplanetary particles near apogee. Thus, many of the magnetospheric phenomena studied by ONR-602 from low altitude in polar orbit can be extended by CRRES, as well as maintaining the capability for measuring solar flare particles and their access to the magnetosphere. In addition, the GTO provides access to regions of the magnetosphere unavailable to ONR-602 and thereby will permit an expanded range of investigations.

The data available from the ONR-602/604 packages consist of pulse height analyzed events and counting rate information, the latter from both the Main telescopes and the Monitor telescope. (Much of the information on magnetospheric particle populations from ONR-602 has been obtained from the Monitor counting rates.) Techniques to handle the ONR-602/604 datasets have been developed for both the compressed rate (CHART) data and the raw, uncompressed (PHRET) data format. In both cases it was necessary to write tape reformatting routines, re-copy all tapes and develop record decoding software. In addition, a software plotting library was developed and will be augmented for the CRRES mission plots.

Understanding counting rate data requires knowledge of the instrument response to the various types of particles encountered in space. This can only be done from the data itself, and a portion of the analysis effort must be directed to this goal. The telescopes return three types of counting rates, the Monitor telescope rates, Main telescope coincidence counting rates, and Main telescope singles counting rates. With

the nominal ONR-602 Main telescope detector thresholds (D1, D2 = 2 MeV; T1, T2, T3 = 4 MeV; K1, K2 = 1 MeV; A = 0.25 MeV; S = 0.5 MeV) and Monitor thresholds (0.35, 2.5, a 10 MeV), the rate data sample protons, helium and heavy nuclei over different energy ranges down to below 1 MeV/nucleon with the Monitor and to above 100 MeV/nucleon with the Main telescope. In addition, a rough measure of energetic electrons can be obtained from the counting rate of the anti-coincidence scintillators surrounding the Main telescopes.

One approach to "calibrating" rates involves intercomparison between two different instruments. Here we have used IMP-8 located in interplanetary space, and Figure 3 shows a comparison of counting rates for the June, 1982 flare period where, for ONR-602, only polar cap data is employed. The top two plots (note logarithmic y axis) give 30-95 MeV proton and ~1 MeV electron rates from IMP-8. The center plot shows the Cherenkov trigger rate in the IMP-8 main telescope corresponding to >100 MeV penetrating protons. The peak at day 156-157 corresponds to the arrival of relativistic particles (>100 MeV protons, electrons). This peak is also present in the ONR-602 SS rate indicating that SS is responding to these same relativistic particles. However, the SS rate does not fall off after this peak nearly as rapidly as does the >100 MeV proton plot. This indicates that SS is observing an additional component, either 50-100 MeV protons or medium energy electrons (with less than 100% efficiency) or, probably, some of both. This intercomparison shows that SS responds to the higher energy particles and may be employed as a monitor.

An additional part of understanding the instrument response is the assessment of the background contribution to the counting rates. This is most severe for singles rates which have a large geometry factor but is non-negligible for coincidence rates as well. Background can arise from detector noise, from electronic problems, from multiple particle events and from sub-threshold particles that undergo interactions or scattering. This was particularly important for the Monitor telescope where preliminary analysis showed unexpectedly high MM and MH counting rates (corresponding to low energy alpha particles and  $Z \geq 4$  nuclei) at low altitude. The possibility exists that some of these counts may be due to large angle, high energy protons penetrating the passive shielding around the Monitor telescope or to multiple low energy particles penetrating "simultaneously."

Again, comparison with IMP-8 can be performed, and Figure 4 shows a full mission comparison of the IMP-8 L1NL2 rate (hourly averages) with the ONR-602 monitor ML rate (polar cap averages). The two rates (from nominally identical detector systems) correlate remarkably well. This is demonstrated for the June, 1982 flare period in Figure 5 where the two rates are superposed. While there are some slight differences, overall the correlation, even for the highest intensity periods, is quite good. This implies that any saturation, background or multiple particle events in ONR-602 must also be present in the IMP-8 system. Alternatively, both systems may be relatively immune to such effects.

To investigate the MM and MH rates, it is necessary to build both the passive shielding and the active detector volumes into a Monte Carlo program. Protons (or other particles) are then simulated, with random directions of incidence and a wide range of

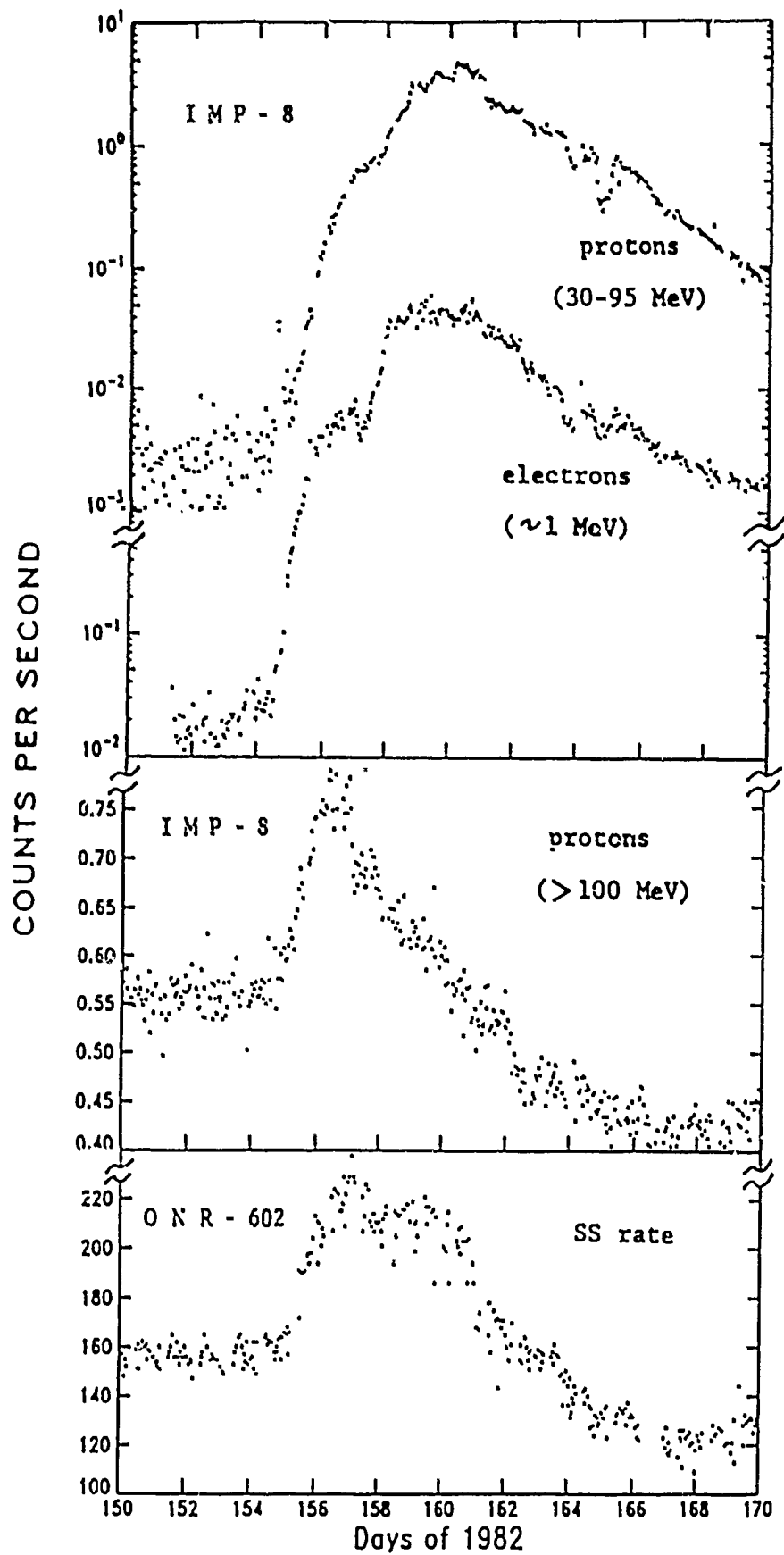


Figure 3. Comparison of IMP-8 "high" energy rates with CNR-602 scintillator rate.

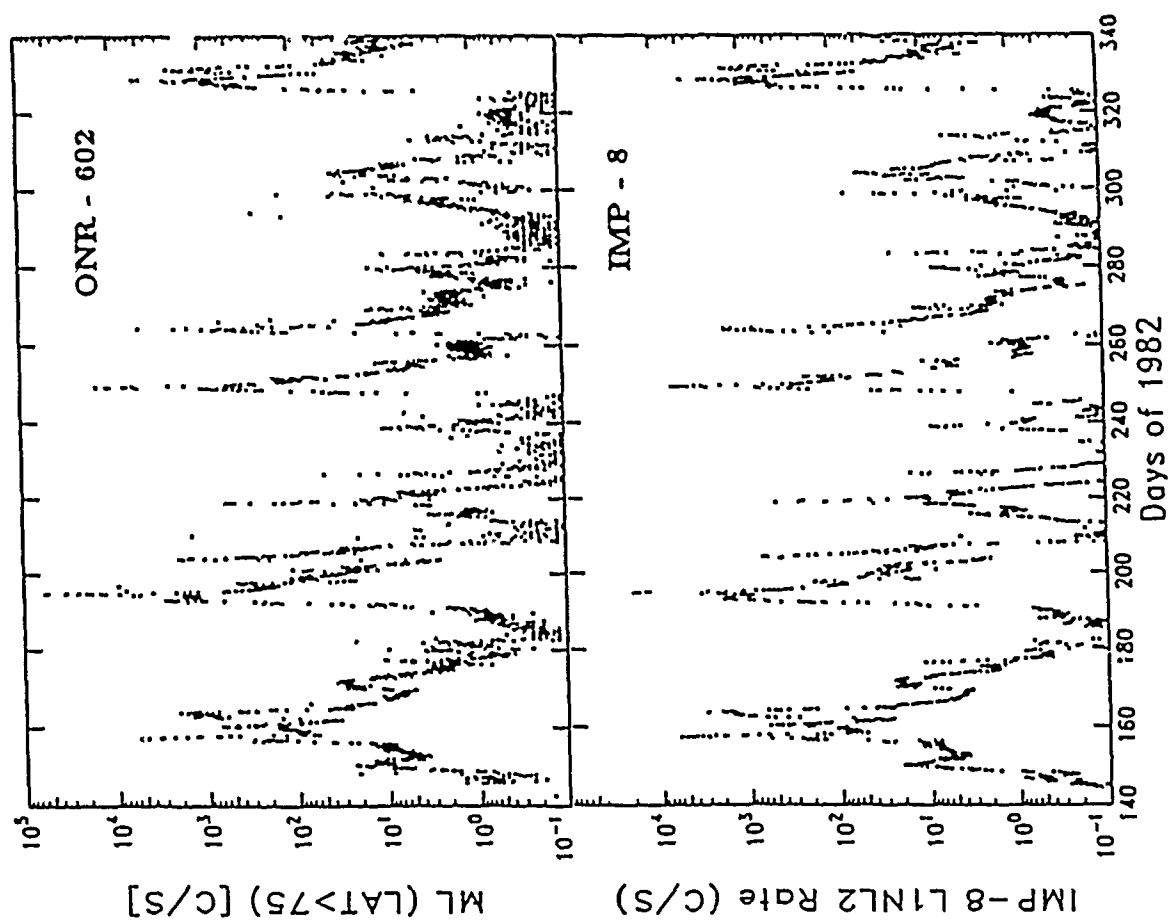


Figure 4. Comparison of IMP-8 and ONR-602.

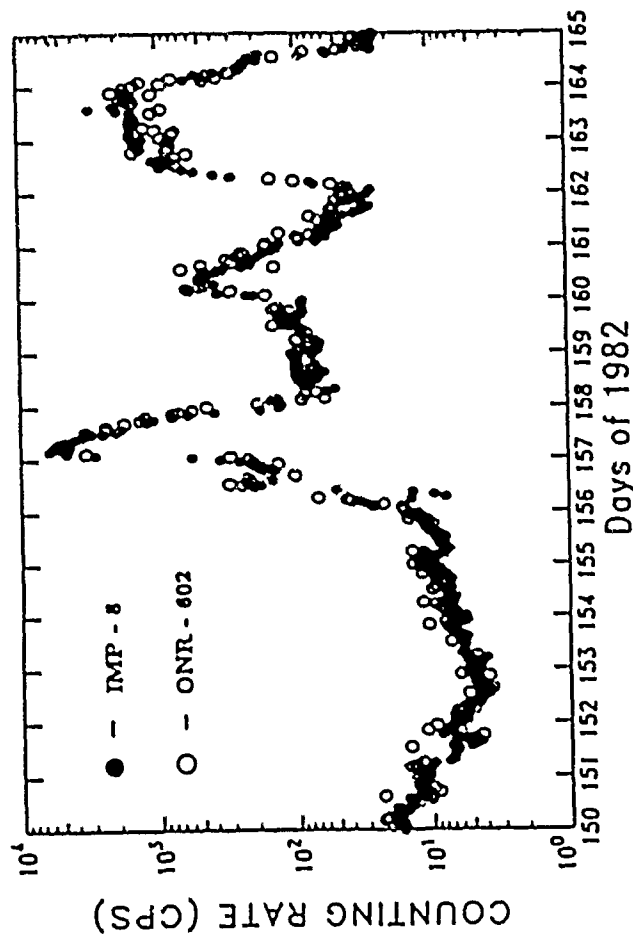


Figure 5. IMP-8 and ONR-602 for the June flare period.

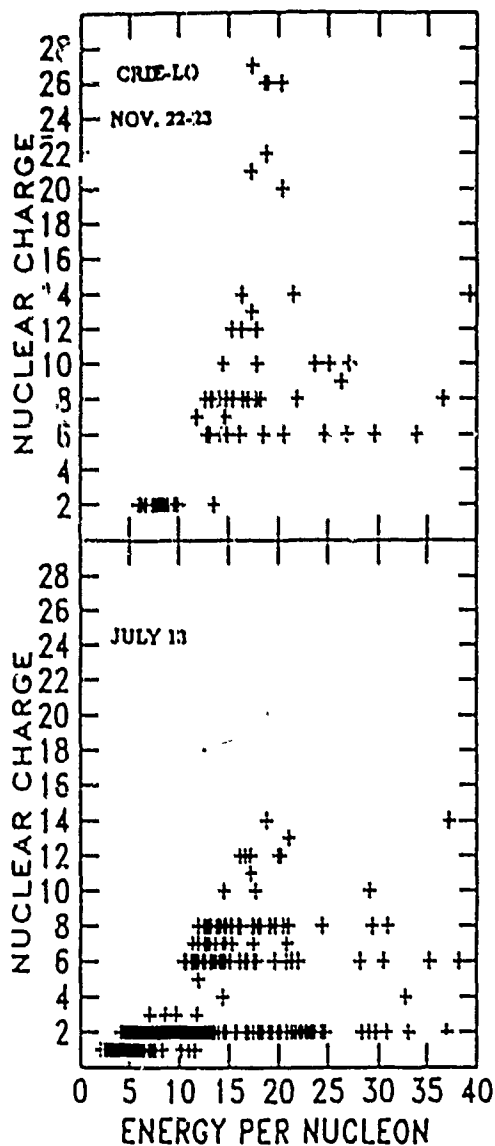


Figure 6.  $Z$  vs  $E$  for two flare periods.

energy, and are followed through the passive shielding into the detector volume, where their signal is calculated. In this way we can isolate, for specific particles and energies, any trajectories through the system which result in signals of a specific level and determine the solid angle of such trajectories. We have found, for example, that protons at energies greater than 90 MeV, and incident at nearly 90 degrees with respect to the Monitor telescope axis (where their path length in the detector is large) are required to make MH counts.

There is also a possibility that during intense solar flare periods the monitor rates may be triggered by multiple particles arriving during the detector response interval whose signals "pile-up" to simulate a real MM or MH count. Such effects have been observed, as well, in the Phoenix-1 main telescope. Figure 6 shows a charge vs energy plot for events recorded in the main telescope for two flare periods, July 13, a very intense flare and Nov. 22-23, a medium intensity period. The main telescope thresholds given above are designed so that protons are never pulse height analyzed. However the 13 July period shows significant numbers of events assigned to  $Z = 1$ . In addition, there are events at  $Z = 3-5$ , elements that should be absent in solar flares. Note that the less intense 22-23 Nov. period shows the nominal telescope response. Thus, we must conclude that particle pile-up was occurring during the intense July 13 flare.

Such effects should be studied in pre-launch accelerator calibrations, as well as by comparisons/correlations between different counting rates and different instruments. This type of accelerator calibration was not done prior to the ONR-602 launch, but has been performed for ONR-604 during a recent (2/89) calibration at the Lawrence Berkeley Bevalac, as described below.

Simulating the magnetospheric environment of CRRES involves providing an intense radiation background such as the satellite will experience. It is not feasible to simulate the proton fluences, but the electron background can be simulated using radioactive sources. We acquired a 100 millicurie  $^{144}\text{Ce}$ - $^{144}\text{Pr}$  beta/gamma source with a  $\sim 3$  MeV beta particle end point and gamma rays of 0.7 and 2.2 MeV. A source

holder/collimator was designed and constructed with provision for mounting such that the source "beam" could be directed at the front of the telescope at an angle of  $\sim 25^\circ$  to the normal (to remove the source holder from the heavy ion beam) while the accelerator beam was incident on the experiment.

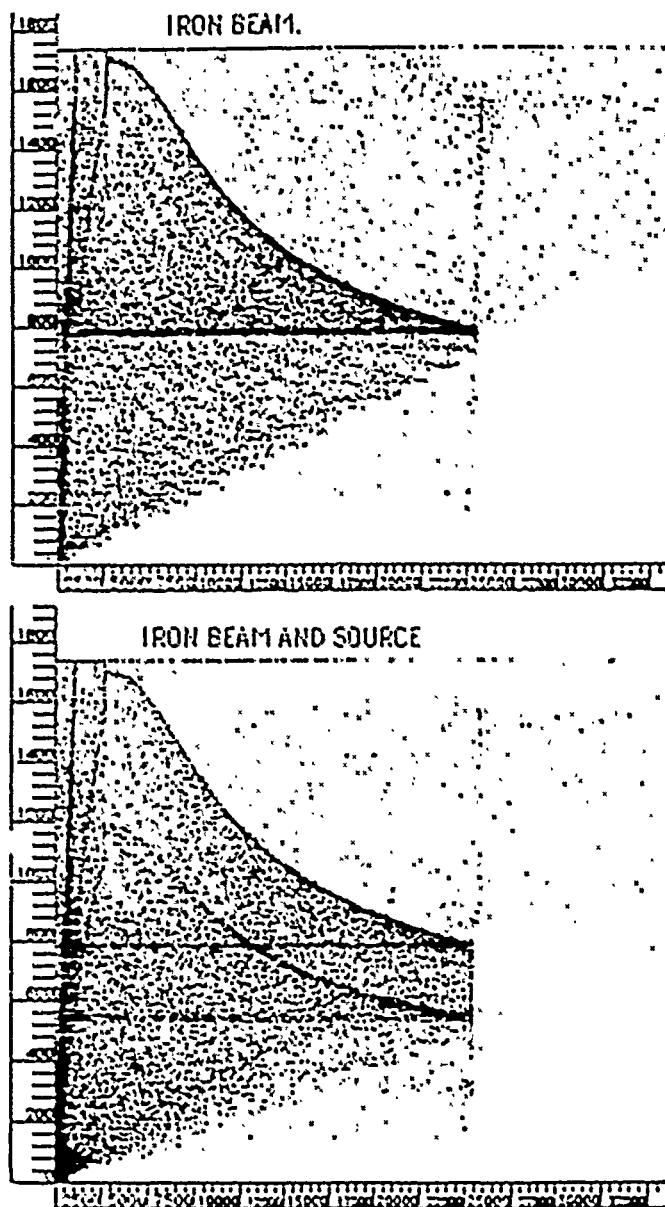


Figure 7. D1D2 vs D3-K8 matrix for CRRES exposed to an  $^{56}\text{Fe}$  beam showing the effect of background radiation.

D2 vs D3-K8, with no anti-coincidence requirement, and there are approximately equal numbers of events in each matrix. The important result is the appearance of the second (ghost) track at a signal level  $\sim 30\%$  below the normal location. This is a direct result of the high rate of firing of the D1, D2 electronics ( $\sim 20,000/\text{second}$ ) stimulated by the source. This results in a baseline shift for some fraction of the events. Recognizing and correcting for such shifts in the ONR-604 flight data during

Several different types of calibration runs were taken. First, with the instrument in the synchronous spacecraft readout mode, the source was used to test the logic systems. Runs were made with the source at different distances and angles from the instrument thereby simulating different background intensities. Runs were taken both with and without the external pulser triggering detectors D1 and D2 and in a variety of instrument operating modes. The results are still being analyzed, but qualitatively it was possible to simulate low energy particles by the electron-gamma pile-up in the instrument.

Additional tests were made with the instrument in accelerator mode with both source and beam operating. An example of the raw data is shown in Figure 7 where the top plot (no source) is to be compared to the bottom plot with the source. In both cases the matrix displayed is D1 +



magnetospheric passes or intense solar flares will be one of the major analysis challenges.

## B. Solar Energetic Particles

The ONR-602 (and ONR-604) instruments are specifically designed for the study of solar energetic particles (SEP) observed in near-Earth space. ONR-602 was launched into the declining phase of the last solar maximum and ONR-604 will be launched into the predicted maximum of the present solar cycle. Figure 8 shows the solar energetic particle events that occurred during the active lifetime of the S81-1 mission. Plotted is the intensity of interplanetary protons >10 MeV as recorded by the GOES monitoring satellites along with an indication of the flare classification. Both individual flare analyses and aggregate solar particle studies have been carried out on these 1982 flares.

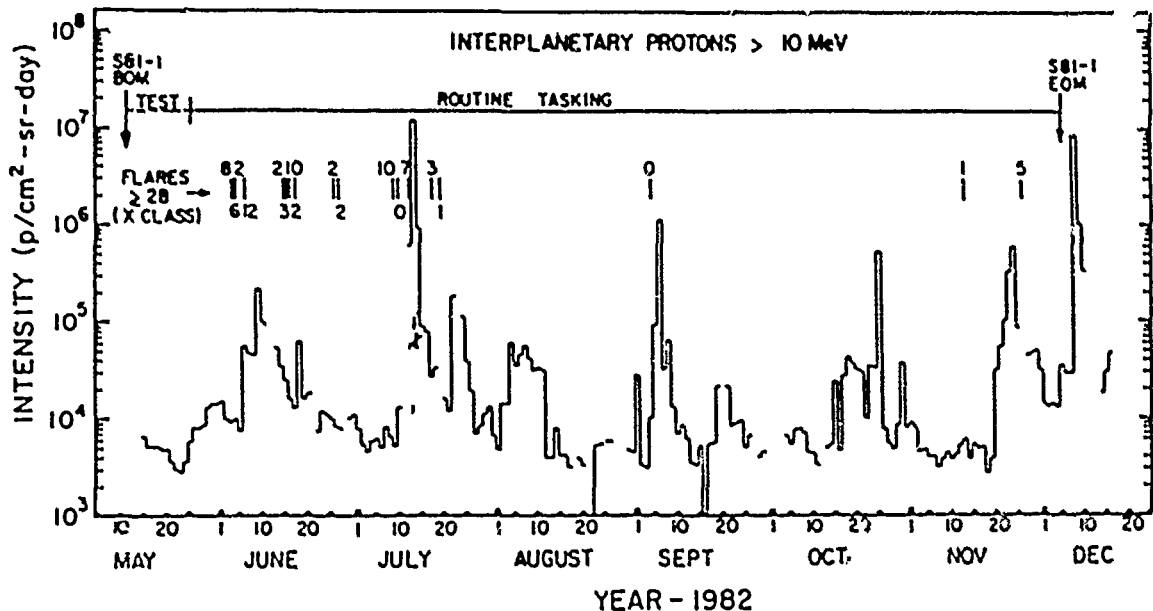


Figure 8. Solar Energetic Particle Events Observed by ONR-602.

**Solar Particle Access:** The question of the access of solar energetic particles to the polar cap regions of the magnetosphere is important for the Phoenix-1 instrument in polar orbit. An interplanetary monitor is provided by the low energy telescope on the IMP-8 spacecraft, and a comparison of the two rates was shown in Figures 4 and 5. The correlation time scale between the two spacecraft is generally  $\leq$  few hours. However, the data for day ~163 suggest periods where correlation times may be as long as 10-12 hours, perhaps due to access from the extended magnetotail. These results confirmed that the ML detector was observing interplanetary particles over the poles.

We can use the ONR-602 data to study more details of the access process. Figure 9 compares the ML and MM counting rates during a North pole pass (top) and a South pole pass (bottom) for day 302 of 1982. The time resolution is 4 seconds corresponding to ~30 km spatial resolution. The wide region of relatively low flux observed across the North pole on the night side indicates inhibited access of interplanetary particles into that zone except at

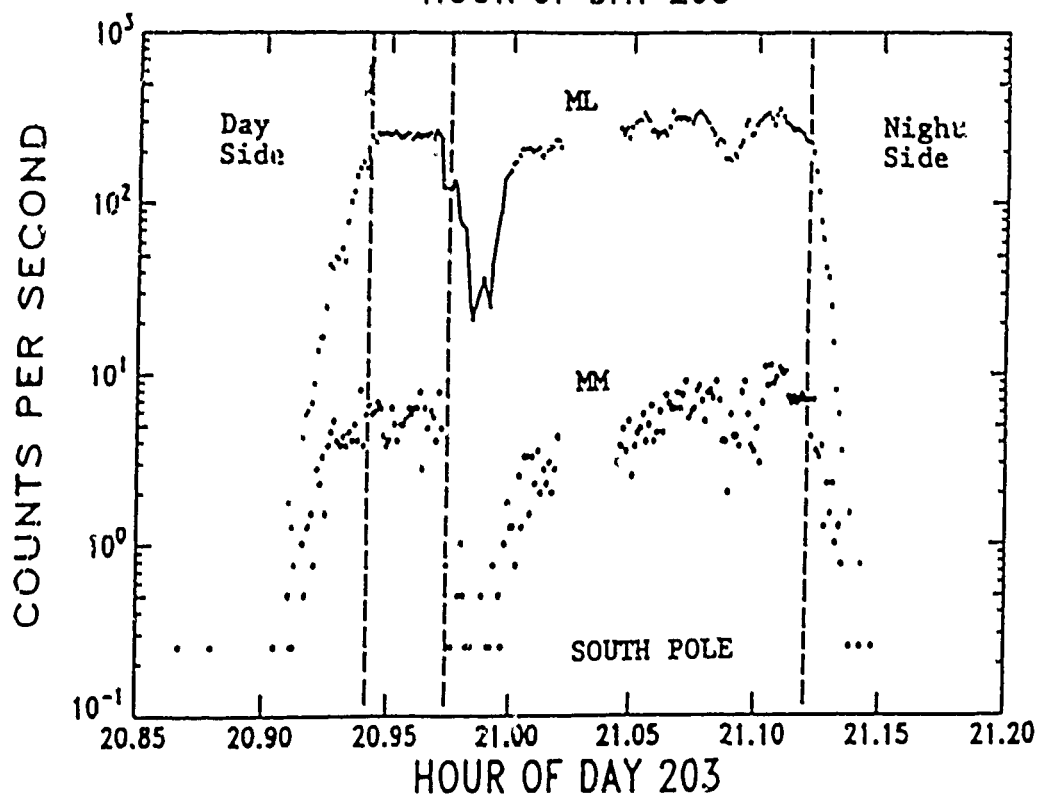
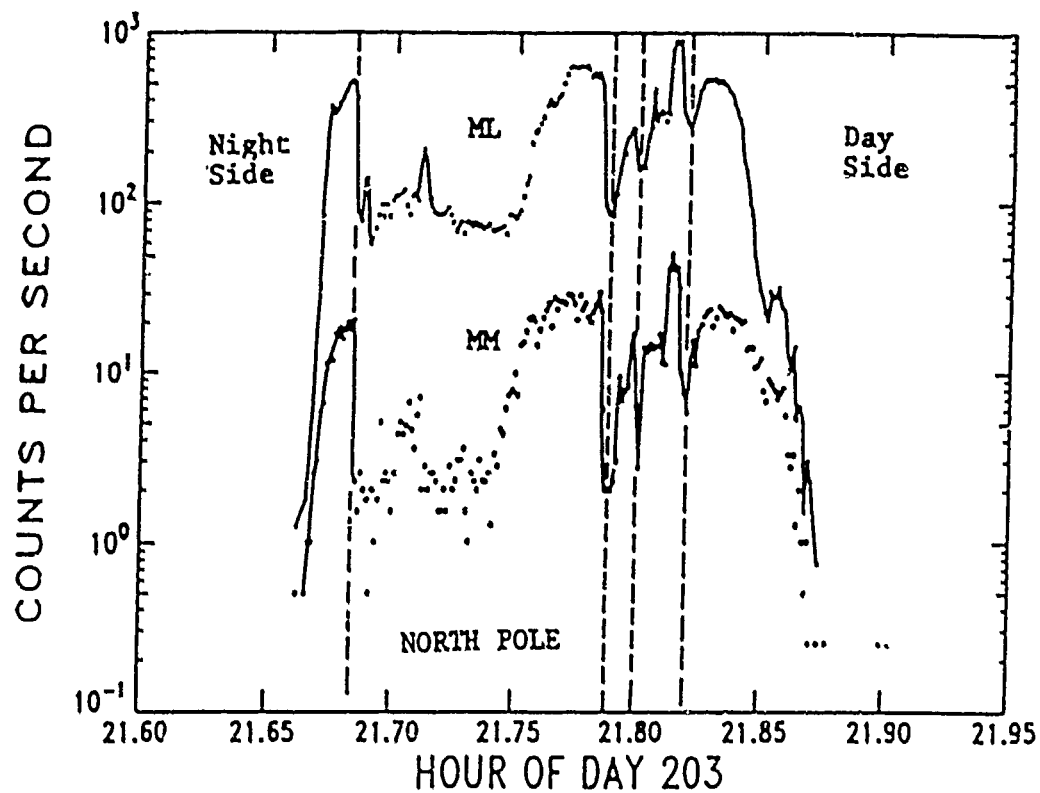


Figure 9. ML (proton) and MM (helium) counting rates during a polar cap crossing over the North pole from the night side to the day side (top) compared to the previous South pole crossing from the day side to the night side (bottom). Interplanetary solar particle fluxes are rapidly increasing at this time.

large distances down the magnetotail, perhaps due to the orientation of the interplanetary magnetic field at that time which may have provided preferential access to the southern polar region. Note that proton and helium counting rates show approximately the same polar cap structure, indicating that we are indeed observing interplanetary particles.

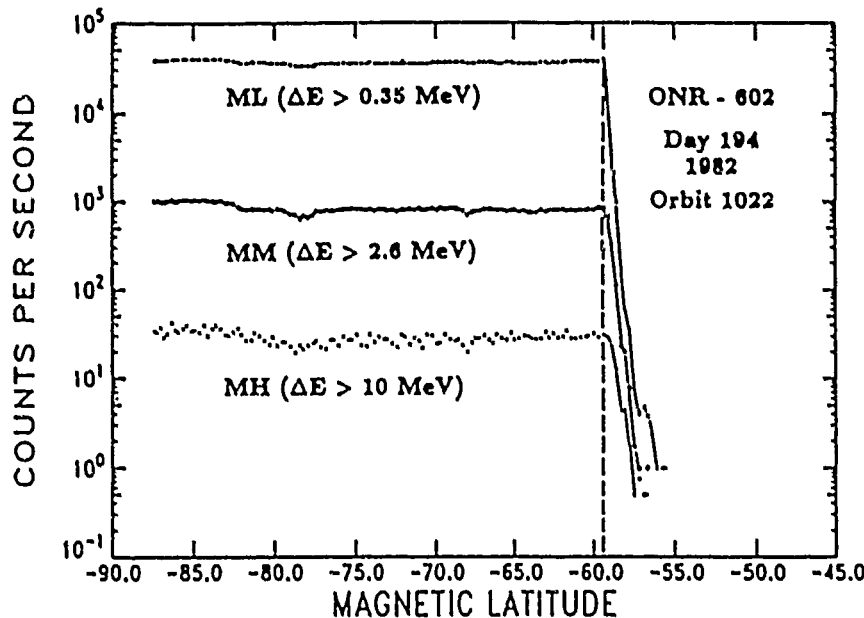


Figure 10. Monitor counting rates for a polar cap pass.

the 3-6 km range. Note that the Stormer cutoffs for the geomagnetic field at the boundary are  $\sim 13$  MeV for protons and  $\sim 3$  MeV/nucleon for helium, an order of magnitude larger than the proton and helium thresholds.

**Flare Composition:** An aggregate analysis was performed for the combined flare periods of June, July and November, 1982 which yielded the overall elemental composition and the isotopic distribution for C, N, O, Ne, Mg and Si. The mass histograms are shown in Figure 11 in which the individual isotopes (e.g.  $^{24,25,26}\text{Mg}$ ) are easily distinguishable. These isotopic results are summarized in the lower part of Figure 12 and compared to other results (Dietrich and Simpson, 1979; 1981; Mewaldt et al., 1983; Simpson, Wefel and Zamow, 1983). The low abundance of the tracer isotopes  $^{13}\text{C}$ ,  $^{15}\text{N}$ ,  $^{17,18}\text{O}$ ,  $^{21}\text{Ne}$  indicates no appreciable secondary spallation component, in contrast to large spallation components in galactic cosmic rays (Simpson, 1983; Garcia-Munoz et al., 1987). The agreement of the measured isotope composition with standard solar system material (Anders and Ebihara, 1982; dashed lines in bottom panel of Figure 12) indicates that particle rigidity is not a dominant effect in the solar flare acceleration process. Rigidity may still play a role, but more precise, higher statistics data will be necessary to determine the size of any effect.

The top panel of Figure 12 shows the correlation (Guzik, 1988) between Solar Energetic Particle (SEP) elemental abundances and abundances derived from solar gamma ray line observations plotted as a ratio of the measured abundance of the elements to the solar system abundance (Cameron, 1982), all relative to Si, as a function of the first ionization potential of the element. The correlation of decreasing relative abundance with increasing ionization potential has been known for several

The sharpness of the proton trapping boundary corresponding to the last closed field line is illustrated in Figure 10 for the low energy proton, helium, and heavy ion counting rates from the Monitor telescope for a period of especially high solar particle intensity. The dropoff in counting rate within one four-second interval gives a plasmopause boundary thickness less than 30 km, which is comfortably wider than the sampled particles' gyroradii which are in

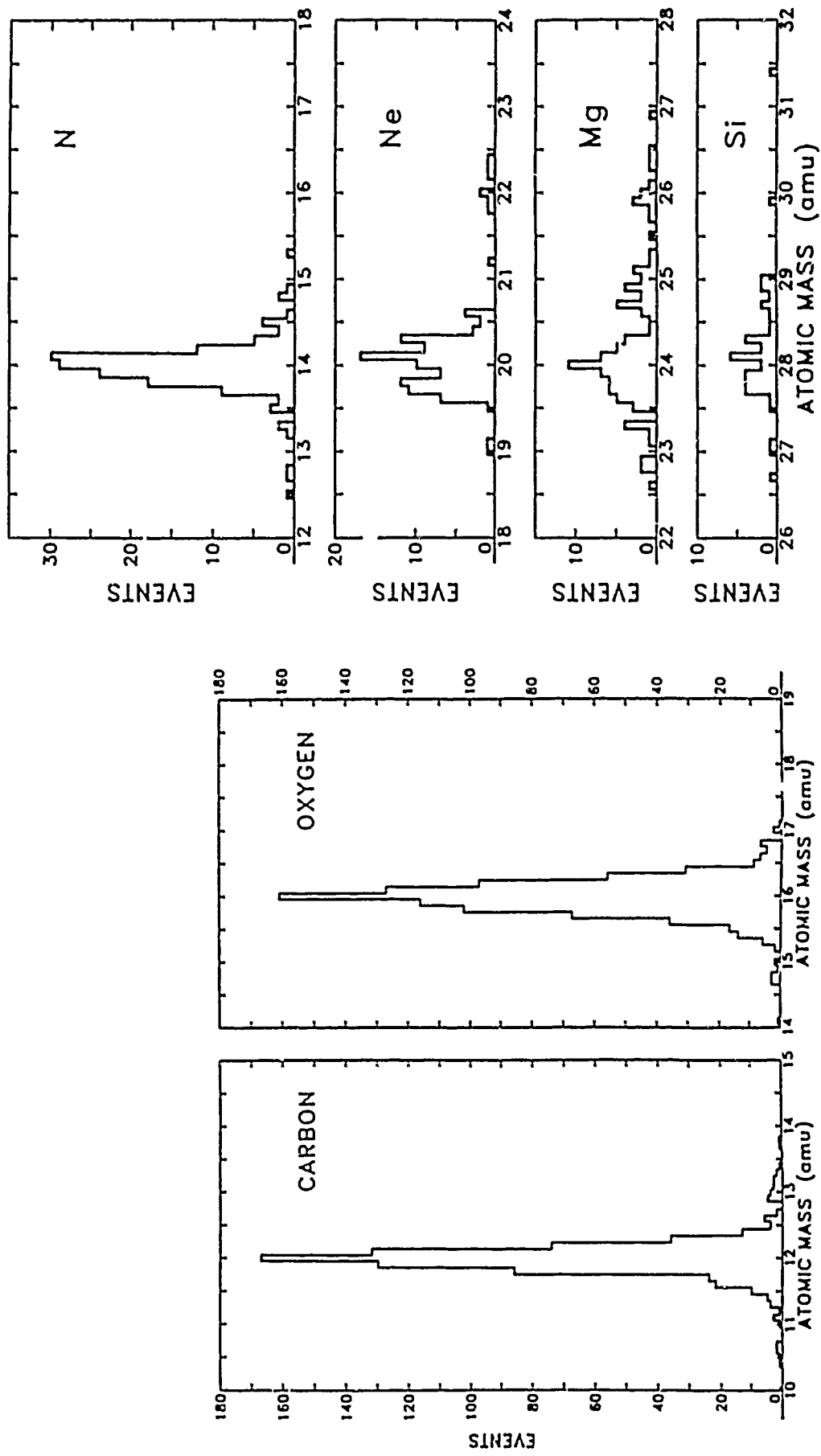


Figure 11. Mass histograms for the sum of the flares observed by ONR-602 in 1982.

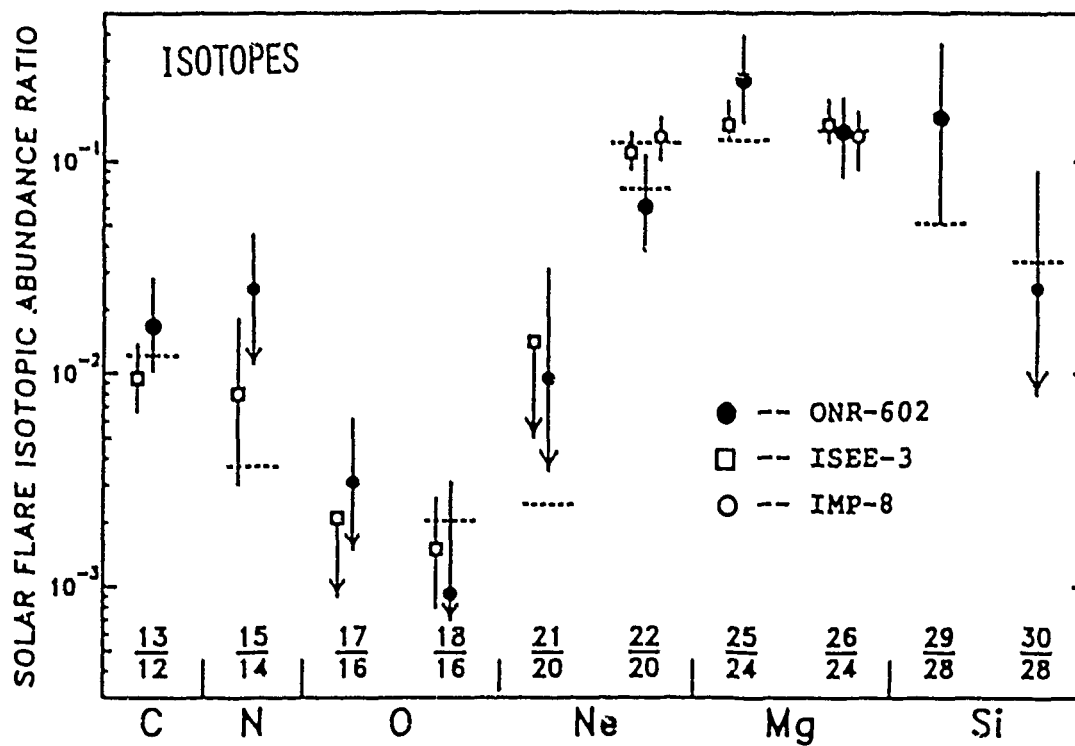
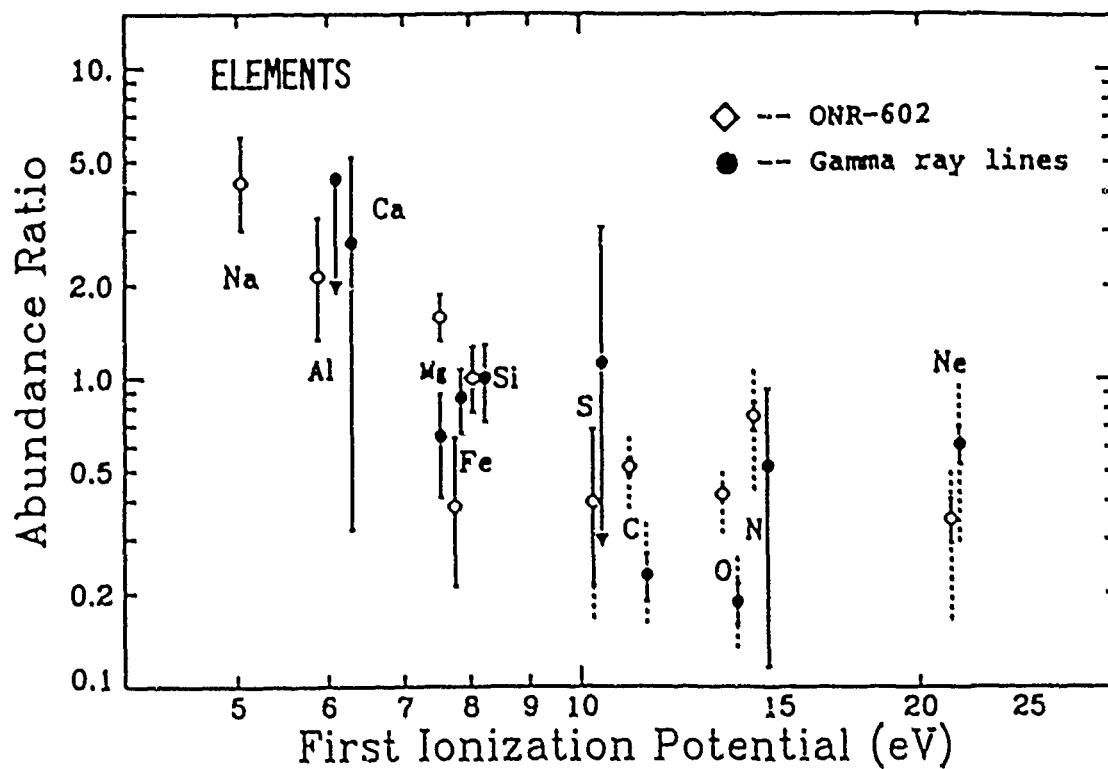


Figure 12. Solar Energetic Particle Abundances.

years (Meyer, 1985) and has been interpreted as evidence for a selection effect in the particle acceleration process, i.e. particles with low first ionization potential are preferentially accelerated. The recent gamma ray line observations (Murphy et al., 1985), shown on the top plot offer a new piece of information. The gamma rays are produced by the decay of excited nuclei that result from nuclear interactions, with the ambient medium, of the high energy particles directed inward from the flare site. The preliminary abundance ratios calculated from the gamma ray data show agreement with the SEP observations. This implies that the first ionization potential selection effect is already present in the ambient matter and is not a property of the particle acceleration process but is part of the physical conditions existing on the sun in the "proto-flare" regions. Additional experimental data are needed to fully explore this emerging picture of the solar flare process, and the importance of correlation studies is clearly indicated.

**The Neon Question:** An element of particular interest is Neon. In the solar system there are several components of neon that have been identified based upon the isotopic ratios. Ne-A is

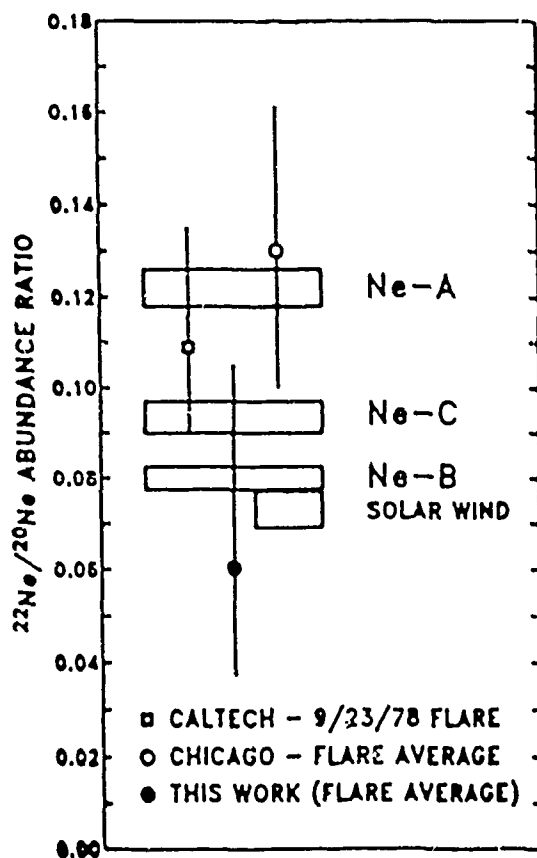


Figure 13. Neon isotopic composition in the solar system and among SEP's.

observed in carbonaceous chondritic meteorites and is believed by some to represent the primordial composition of the solar system (Cameron, 1982). Ne-B is found implanted in the surface layers of meteorites or lunar samples and is believed to be almost the composition of the neon carried by the solar wind. Ne-C is found in lunar samples and is believed to be implanted by solar flare particles (Black, 1983). Thus, there is an open question as to what is the isotopic composition of neon in the sun.

Figure 13 shows these neon components along with a summary of measurements made on SEP's. The older measurements favored Ne-A for the SEP composition, but the Phoenix-1 observations are considerably lower, more like Ne-B or solar wind neon. A weighted average of the three measurements in the Figure would be most consistent with Ne-C but cannot firmly exclude Ne-A or Ne-B as the flare composition. None of the measurements have sufficient statistical accuracy to resolve the question of the exact neon composition in the Sun. Additional data, possibly from the

ONR-604 instrument on the CRRES mission or from a new mission for an instrument such as Phoenix-1, will be needed to solve this longstanding problem.

**Flare Neutrons:** Neutrons provide an additional tracer of the solar flare process. Neutrons produced during a solar flare will decay in-flight and have been observed as

a pulse of protons in interplanetary space (Evenson et al., 1983). The 3 June 1982 solar flare was one in which neutrons were observed, as shown in Figure 14 from the ISEE-3 satellite. (The dashed arrow indicates the arrival of the pulse of neutron decay protons at the ISEE-3 spacecraft.) The ONR-602 data has been analyzed in detail for this flare period, looking at various rates and at data from both the polar regions and

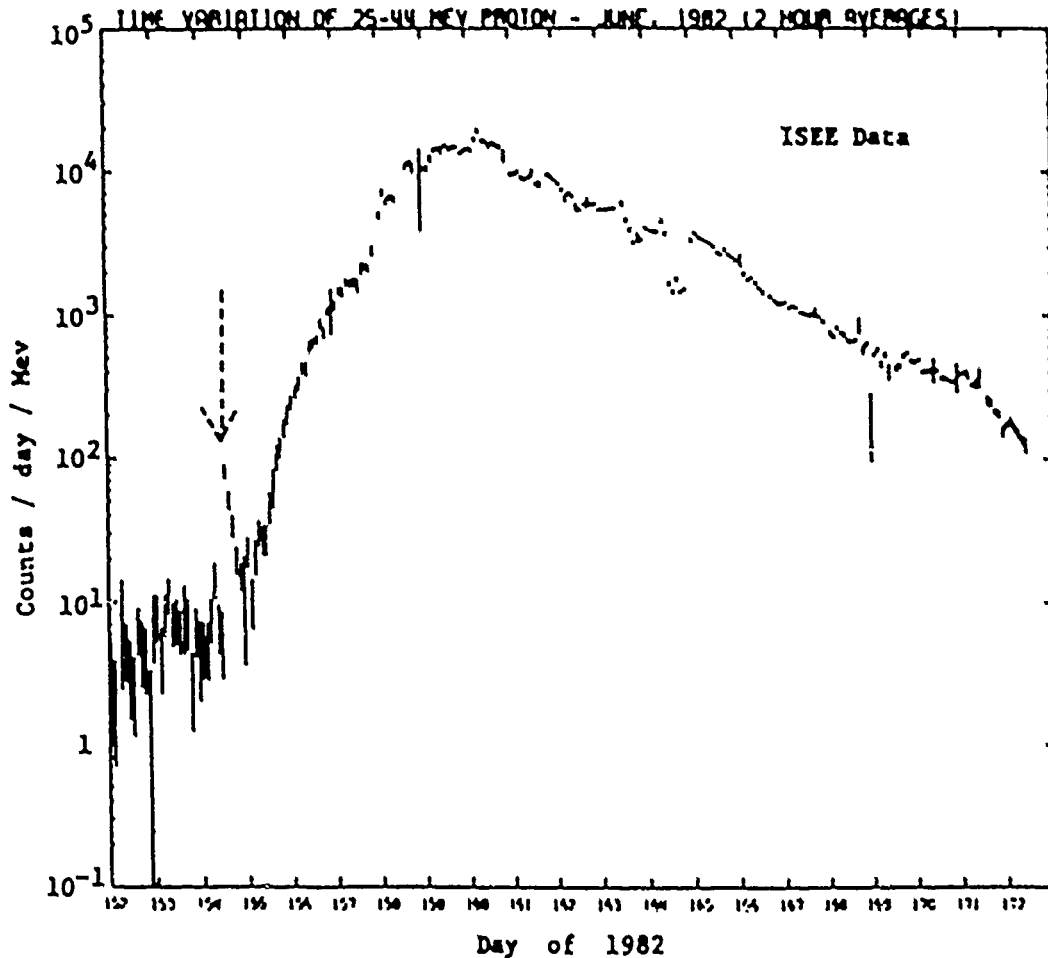


Figure 14. Counting rate of 25-44 MeV protons from the ISEE-3 spacecraft for June, 1982. The arrow marks the proton "pulse" from neutron decay.

mid-latitude regions. No convincing peak in the ONR-602 counting rates was observed. The reason for this is inherent in the Phoenix-1 instrument. The energy range for the particles studied by ONR-602 is too low to observe the decay protons, which were seen between 25-45 MeV in interplanetary space. The discovery of a pulse of protons corresponding to neutron decay, either trapped or quasi-trapped in the Earth's magnetosphere, would be an observation of great importance, since this would be a direct observation of a neutron injection source for magnetospheric particles. Such an investigation should be possible with the higher energy ONR-604 instrument on the CRRES mission.

**Heavy Ion Enrichment:** Flares show large variations in composition (Cook et al., 1984) with some events showing enhancements of the heavy ion component (Mason et al., 1983). For the 1982 flares observed by Phoenix-1, we have compared the large

event of 13 July with the smaller flare of 22-23 November. Using the main telescope, the charge and energy of each pulse height analyzed event were determined and these were shown in Figure 6. Note the much larger number of He and CNO events in the July 13 event. Here the Carbon spectrum, fitted to a power law, appears to fall as  $E^{-4}$  while the oxygen falls as only  $E^{-3}$ . The November flare is consistent with these dependences, but the statistics are meager.

Despite the smaller total number of events in the November flare, 7 particles were detected with a charge of  $Z \geq 20$  compared to no such events in the July period. In the 17-20 MeV/nucleon interval the Fe + Ni/CNO ratio is about unity, compared to an expected ratio of 0.1, which classes this flare as very "Hi-Z enhanced." Note that the threshold energy for observing Fe + Ni is  $\sim 17$  MeV/nucleon and, since most of the events are clustered near threshold, a steep energy spectrum is indicated. Heavy ion enrichment has been correlated with flares of the impulsive type (Reames, 1990) which are also, generally,  $^3\text{He}$  rich, electron rich and proton poor. Our 22-23 November flare is consistent with this pattern. Clearly, larger statistics and a larger sample of SEP events are needed to be more quantitative, and this will be one of the tasks for the ONR-604 instrument during the CRRES mission.

Terrestrial Effects: It is well known that solar flares can have major effects on the Earth and induce storms in the terrestrial magnetosphere. Several such situations occurred during the S81-1 mission, one of which is illustrated in Figure 15. The plot covers about two weeks in July, 1982 with the top panel showing an almost 4 order of magnitude increase in the low energy protons observed by the GOES monitoring satellite. (Only daily averages are plotted and the dashed lines represent missing data.) The ONR-602 main telescope rates responded to this flare during polar cap crossings as indicated in the middle panel. Successive rates correspond to deeper penetration into the telescope, from D1 to D2, T1, T2 and even into detector T3. The peaks in the low energy particle intensities are time correlated with the onset of the geomagnetic storm (lower panel) which peaked on day 195 and lasted for most of the following week.

### C. Trapped Particles

The S81-1 polar orbit gave access to several different regions of the magnetosphere, at low altitude, and provided an opportunity to study the trapped particle populations and their time variations. The S81-1 mission, however, did not provide complete coverage of the globe (due to power limitations on the spacecraft) so that certain regions have only marginal data.

Figure 16 shows examples of the spatial structure of the observed radiation. Here the world grid is  $1^\circ \times 1^\circ$ , and a black spot indicates at least one non-zero readout in that bin. The plot at the upper left shows regions (white areas) over which no readouts were obtained. The other three plots show low energy ( $\sim 1$  MeV) protons (lower left) from the Monitor Telescope ML rate, low energy ( $\sim 1$  MeV) helium (upper right) from the monitor MM rate and medium energy electrons (lower right) from the Main Telescope scintillator rate, SS. Other than the polar regions, where solar flare particles are observed, the most pronounced features are the South Atlantic Anomaly -- SAA -- (protons, alphas and electrons) and a "belt" of low energy protons following roughly the geomagnetic equator. Note that a strong



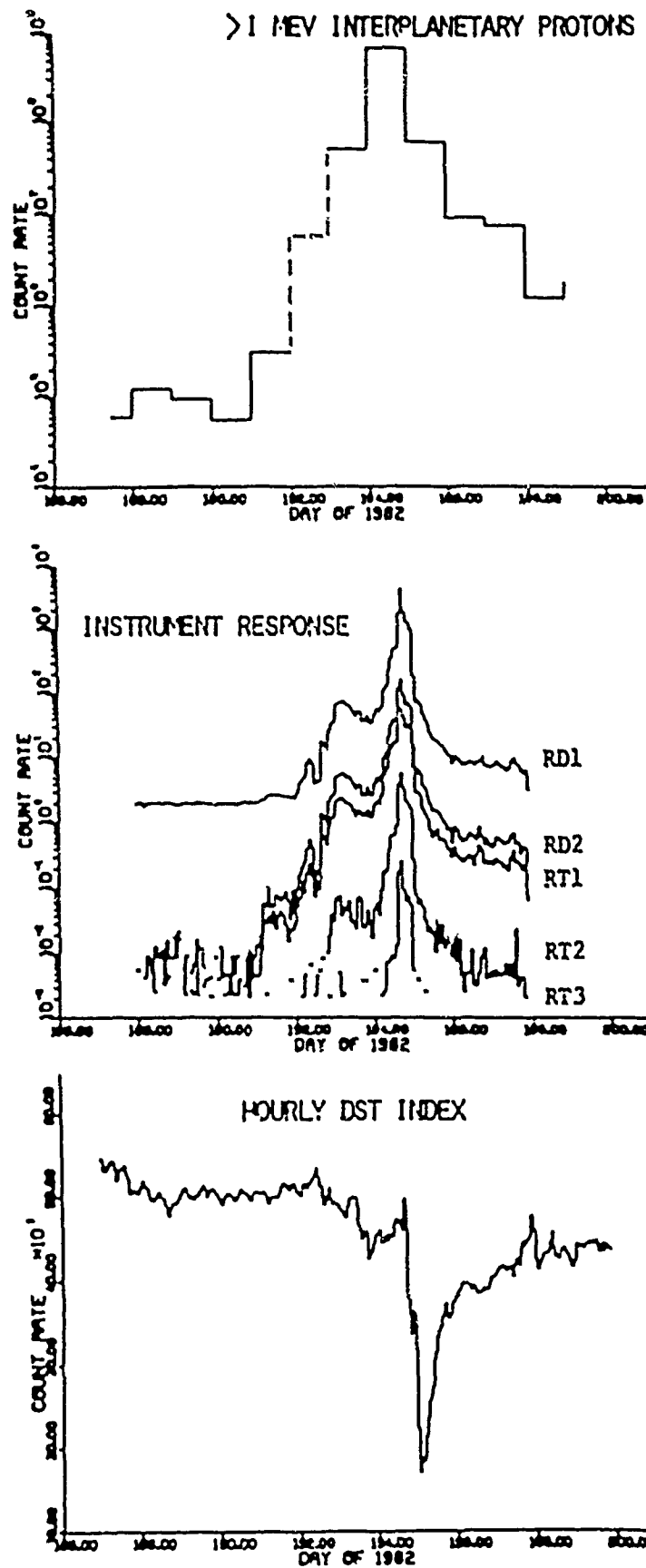


Figure 15. Counting rates for 6-18 July 1982 compared to the geomagnetic Dst index.

electron signature is also seen in the magnetosphere at higher latitudes than the SAA in the southern hemisphere but not in the northern hemisphere.

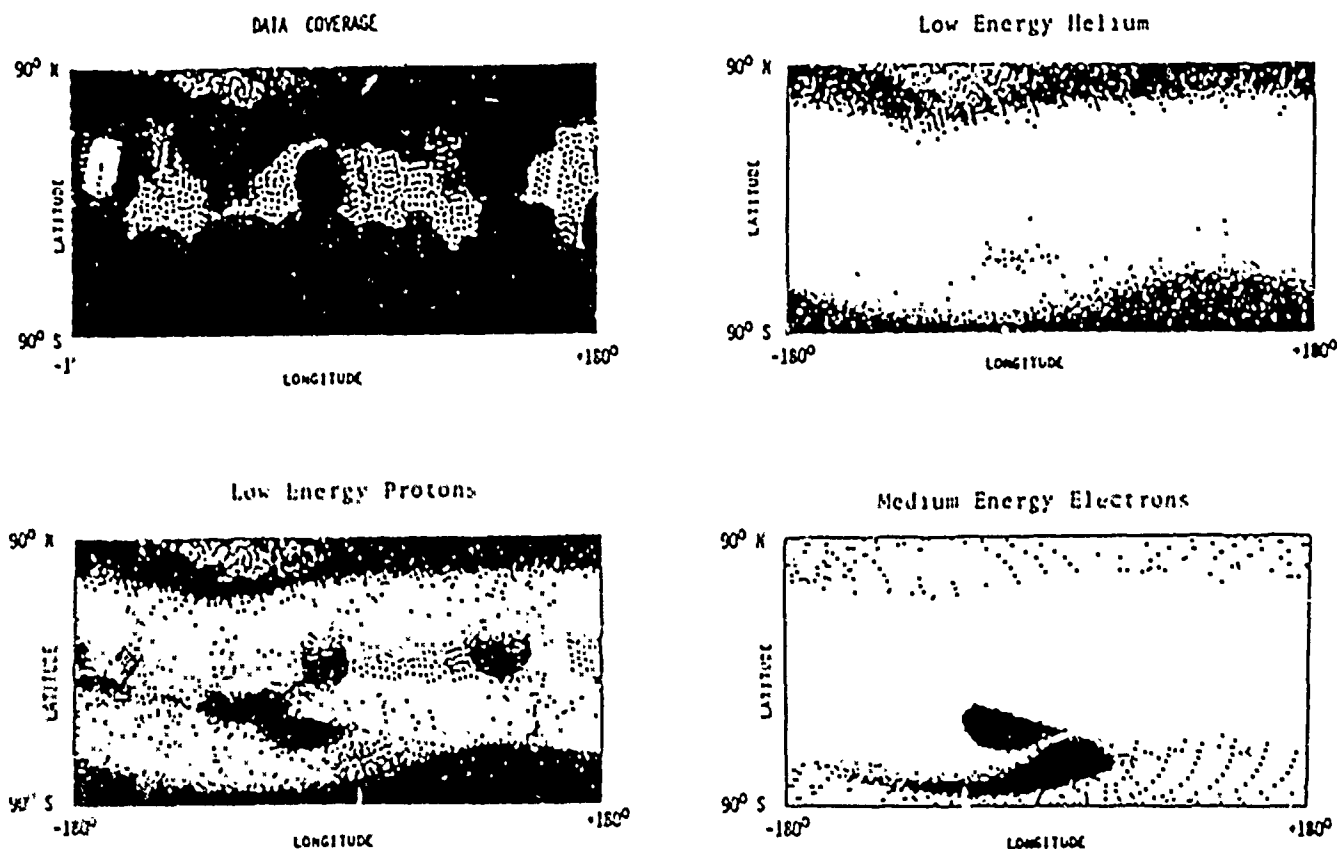


Figure 16. Global plots for energetic particles.

The equatorial belt protons have been observed previously in the late 60's/early 70's (Krassovsky et al., 1964; Heikkila, 1971; Hovestadt et al., 1972; Scholer et al., 1975; Berko et al., 1975) for energies generally in the keV range and were interpreted as a permanent, albeit somewhat variable, component of the Earth's magnetosphere. The observations of this belt by ONR-602 at relatively high energy and by the SEEP experiment (also on the S81-1 spacecraft) at keV energies (Voss et al., 1984) in 1982 shows that this low altitude equatorial belt is, in fact, a permanent part of the Earth's radiation environment.

We can investigate the spatial structure of the electron signature in more detail using different thresholds on the SS rate. This approach is illustrated in Figure 17 where three different levels of SS counts per readout are employed in the plots. At a level of 400 or more counts per readout the SAA and the polar cap are prominent. At increasingly higher intensity thresholds, the polar caps begin to fade leaving the SAA and the southern hemisphere feature. At the highest threshold, only the central part of these features remain. The high electron intensities represent the outer electron radiation belt which dips to low altitudes near the SAA, providing ONR-602 an opportunity to study these particles.

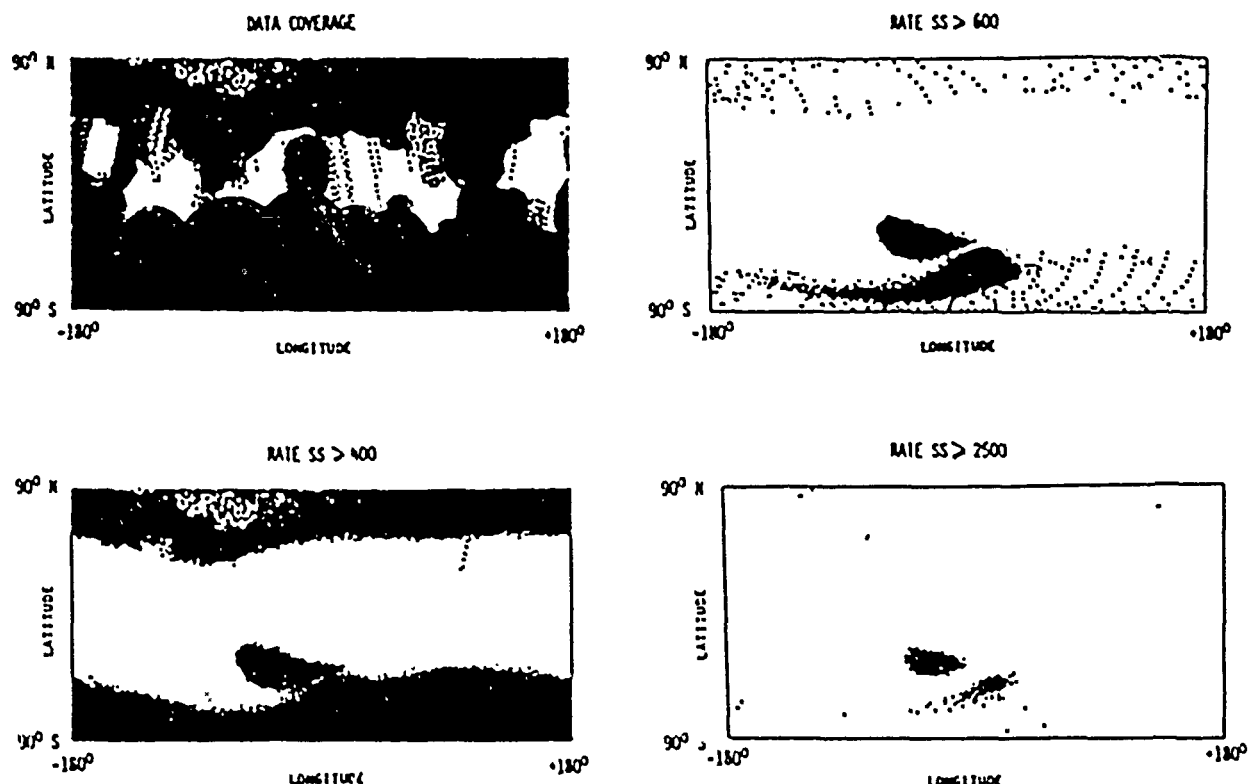


Figure 17. Spatial dependence of the electrons from the SS rate.

The SAA Region: Particle measurements in the South Atlantic Anomaly (SAA) remains an important area of investigation since it is during SAA passes that low altitude spacecraft accumulate much of their radiation dose. The proton and electron components of the SAA have been studied by rockets and spacecraft in previous epochs, but the question of heavier particles remains controversial. Figure 18 displays 4 day averages of the counting rates for ML, MM and MH taken in the SAA. Note that all three rates show the same time dependence, which is also observed in the scintillator (SS) counting rate (not shown). The relative intensities show about 3% helium and 0.2% heavy ions compared to protons, results that are considerably larger than one would expect at these energies. At higher energies few helium or heavy nuclei were pulse height analyzed in the main telescope.

Another test of the data is provided by the L distribution of the counting rates. This is shown in Figure 18 (right) for the Monitor rates. Note that the data encompass both the inner region at  $L < 2$  and the edge of the outer zone at  $L > 2$ , for which the rate increases with increasing L value. This is what would be expected from the Van Allen belts, and we conclude that we are seeing the dipping of the belts to low altitudes in the vicinity of the SAA. While not obvious on the figure, the peak shifts to higher L for MM compared to ML and for MH compared to MM. This may be evidence for the increasing importance of atmospheric loss processes with increasing charge of the particle.

There have been previous observations of heavy ions in both the inner and outer regions (Van Allen, Randall and Krimigis, 1970; Hovestadt et al., 1978; Blake, Fennell and Hovestadt, 1980; Fritz and Spjeldvik, 1981; Spjeldvik and Fritz, 1978; 1981a; 1981b; 1981c) most of which were concentrated at energies below the ONR-602 data and at higher L values. Much of this work comes from the instrumentation on the equatorially orbiting Explorer 45 spacecraft, but observations have been reported from other spacecraft as well (INJUN, S3-2, ISEE). The ONR-602 results provide complementary data to extend the previous results and to be used to compare to models for heavy ions (e.g. Spjeldvik and Fritz, 1978).

The time dependence shown in Figure 18 reflects the state of the magnetosphere and the influence of solar flare events. For the latter part of the mission, Figure 19 shows an expansion of the time base plus the SS counting rate (note logarithmic scale) for SAA

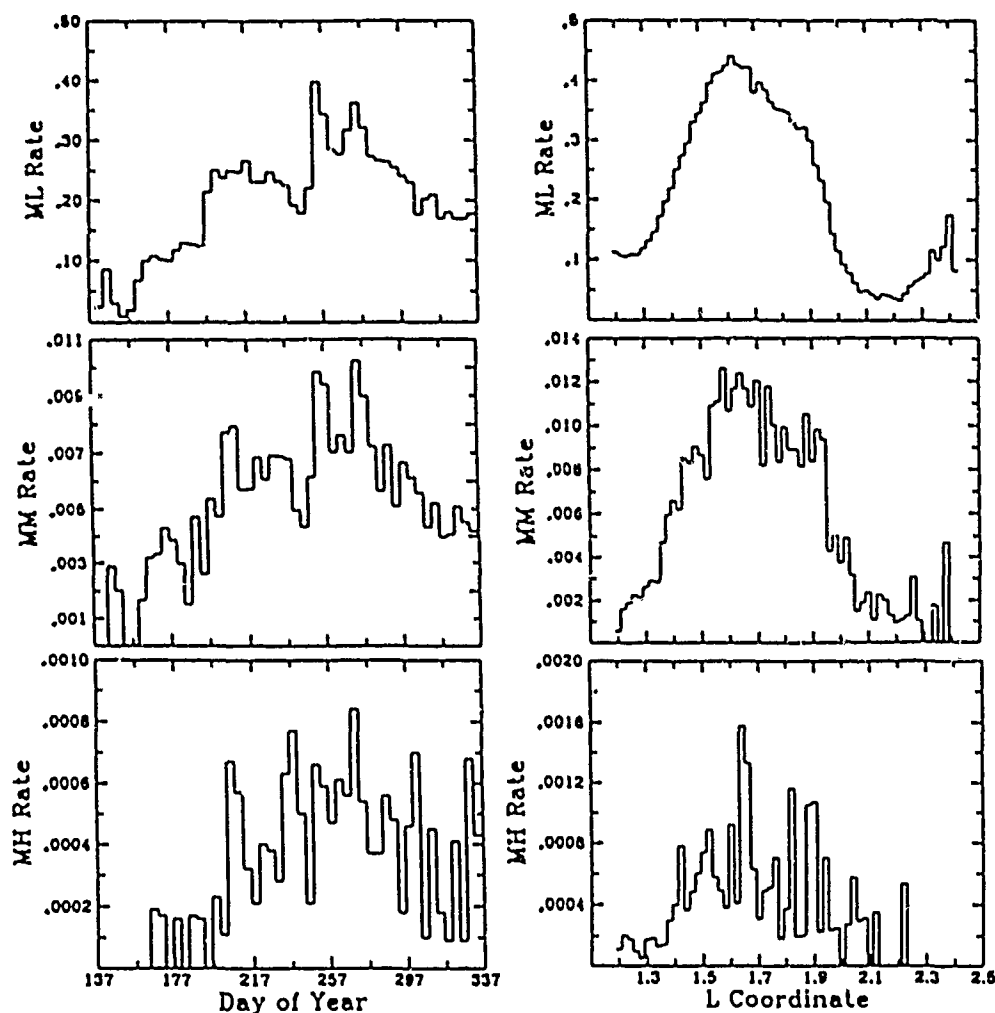


Figure 18. Monitor Counting Rates in the SAA as a function of time (left) and L coordinate (right).

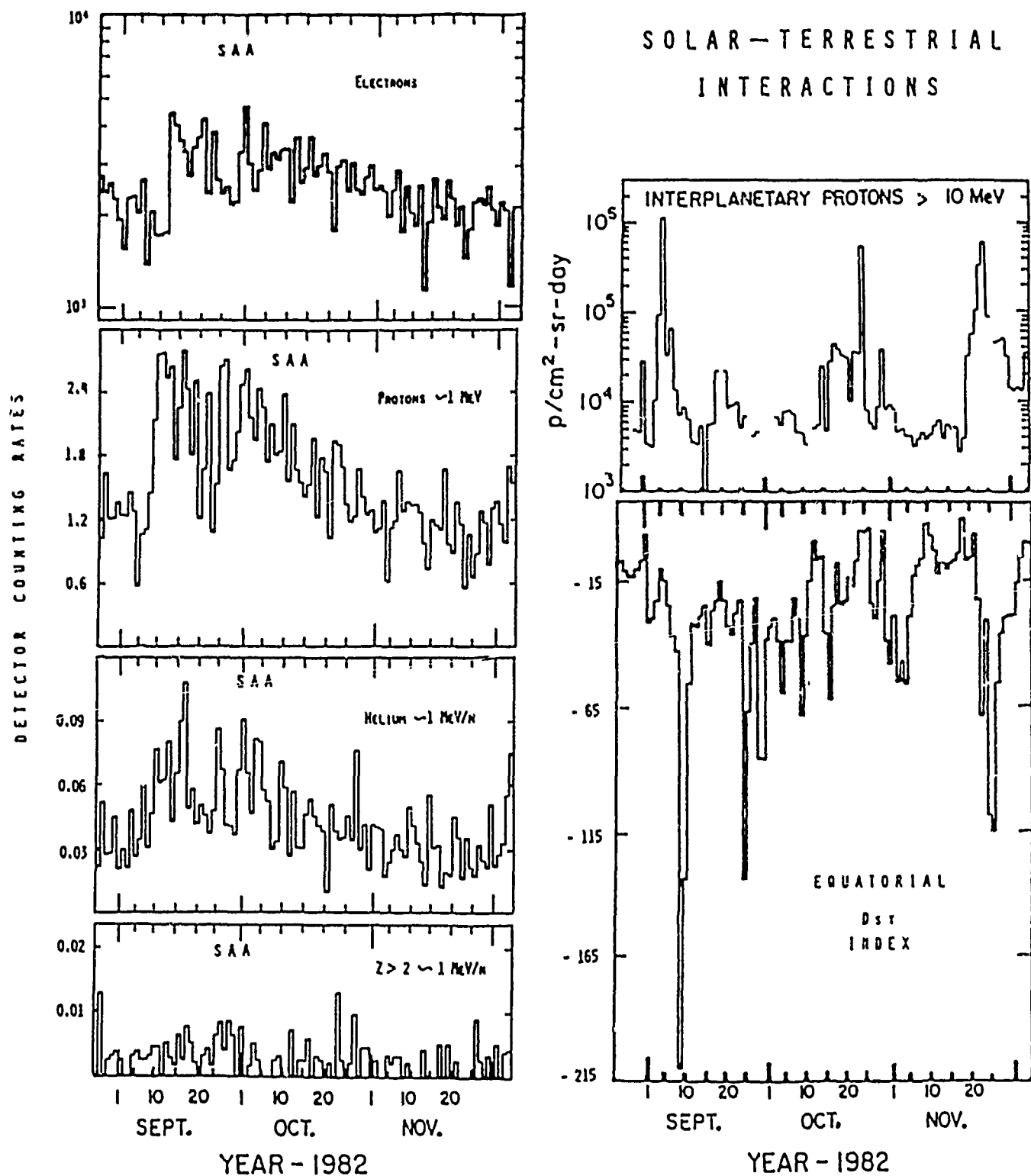


Figure 19. Correlation of SAA measurements to solar flares and geomagnetic storms.

passes. This is compared to the  $>10$  MeV interplanetary protons and the Dst index on the right of the figure. Note that the increase in ML and MM counting rates follows the maximum excursion in the Dst index. This opens the possibility that the particles being observed in the SAA are not stably trapped but are transient, possibly injected by the flare that triggered the geomagnetic storm. Following the injection, the particles appear to "decay" back to their pre-storm levels on time scales of 1-2 months. Whether or not this explanation is correct depends upon the injection mechanism and detailed time correlation between the particles and the magnetospheric conditions.

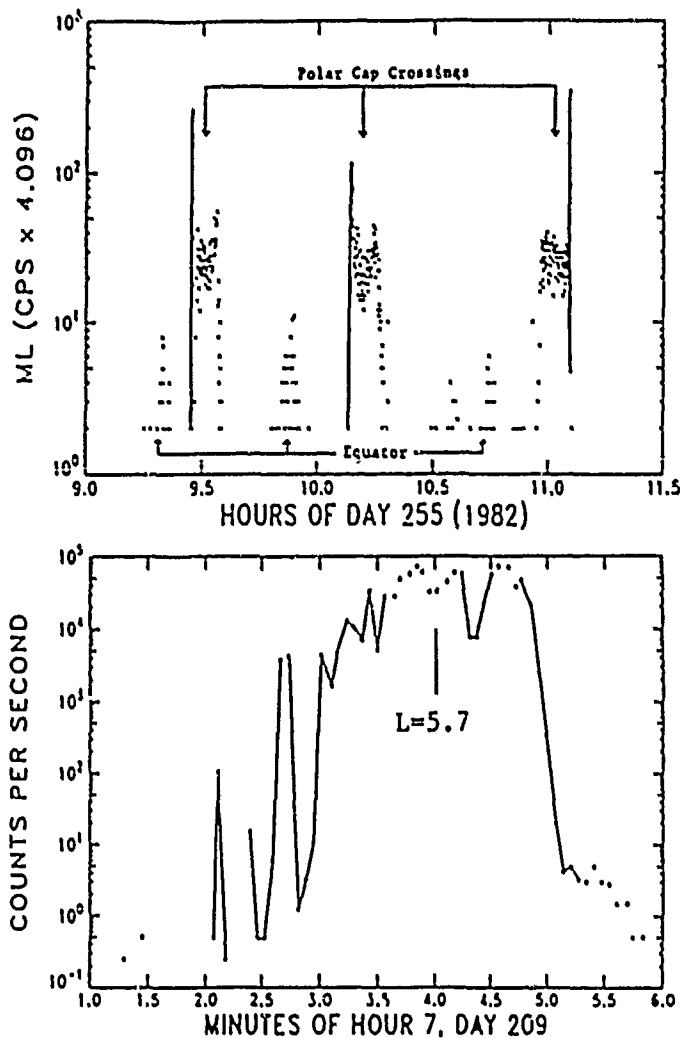


Figure 20. Electron precipitation events.

monitor detector is most likely responsible for the ML spikes. Note that the  $L = 5.67$  location of the spike would be consistent with a large increase in energetic electron flux and/or strong pitch angle scattering near geosynchronous orbit. There is also a possible time correlation to the hard, field-aligned electron component above 600 keV observed in this L-region.

**Equatorial Protons:** The low altitude equatorial regions of Geospace contain a significant flux of precipitating protons as illustrated in Figure 16. The origin of this equatorial belt is traditionally ascribed to charge exchange on the particles in the ring current, leading to neutrals which diffuse downward until they are re-ionized in the thermosphere and

**Electron Precipitation:** Figure 20 (top) shows several orbits of the S81-1 spacecraft during day 255, a period of moderate solar activity. Plotted is the ML counting rate corresponding, nominally, to  $\geq 0.5$  MeV protons. The equatorial belt is indicated as are the polar cap regions. A large precipitation spike is observed just to the side of the polar caps near the plasmaspheric boundaries of the last closed field line. One of the largest spikes (from day 209) is shown in expanded time scale at the bottom of Figure 20. Note that no corresponding spike (or any, significant level of events) was recorded in the helium channel, which strongly suggests that the spikes originate from a nonsolar energetic particle population. A check of simultaneous data from the LPARL medium energy electron spectrometer on S81-1 shows that this was a period of intense electron precipitation at  $\sim 100$  keV. The LPARL instrument was in saturation during most of this period. Thus, it is probable that electron pile-up in the  $40 \mu\text{m}$  thick

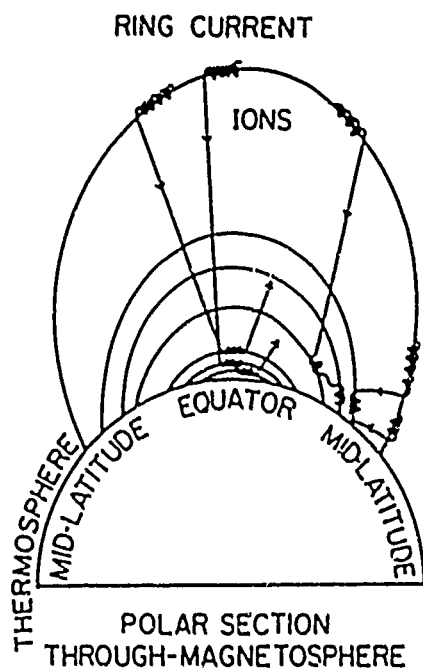


Figure 21. Particle precipitation process.

interpretation of these results are that the particles are "trapped" near the altitude of observation rather than diffusing inward from a higher altitude region. This implies that the process of charge exchange/neutralization followed by restripping/trapping continues down to the altitudes sampled by the S81-1 mission.

become trapped in the lower magnetosphere as illustrated, schematically, in Figure 21. Various analyses (e.g. Moritz, 1972; Berko et al., 1975; Tinsley, 1976; 1979) have used this model to extrapolate measurements back to the ring current and to suggest the presence of alpha particles in this pseudo-belt. The exact nature of the interactions responsible for the charge exchange and the restripping have not been fully specified. It is clear, however, that magnetic storm conditions should affect the intensity of the equatorial belt radiation in a manner similar to their effect on the ring currents.

The many equatorial passes made during the S81-1 mission provided an opportunity to investigate the location of the maxima in particle flux at altitudes well below those of previous missions. Binning the data in  $10^\circ$  longitude bins, as illustrated in Figure 22, produces sharp peaks whose center can be well located in geomagnetic latitude. The FWHM of these peaks is  $8-10^\circ$ . This width is somewhat narrower than observed in previous experiments, giving no indication of diffusive broadening. Thus, the

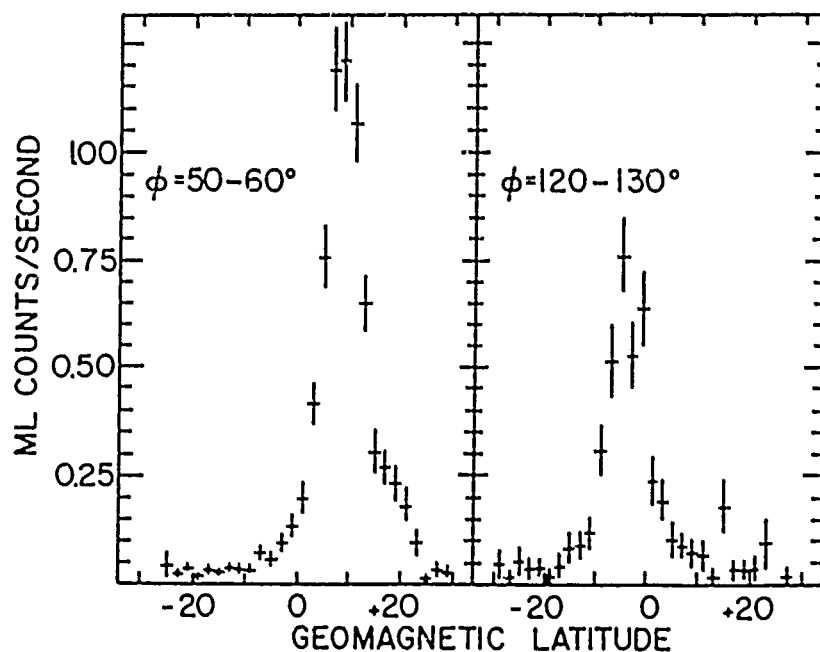


Figure 22. Latitudinal profile.

Figure 23 compares the location of the precipitating particle flux maxima to the minimum-B equator and to EUV observations. The experimental data are in good agreement with the position of the minimum-B equator and with measurements at higher altitude by previous investigators who observed peaks at the equator or at the minimum of  $B/B_0$ .

Prölss (1973) attempted to use the charge exchange mechanism to calculate the

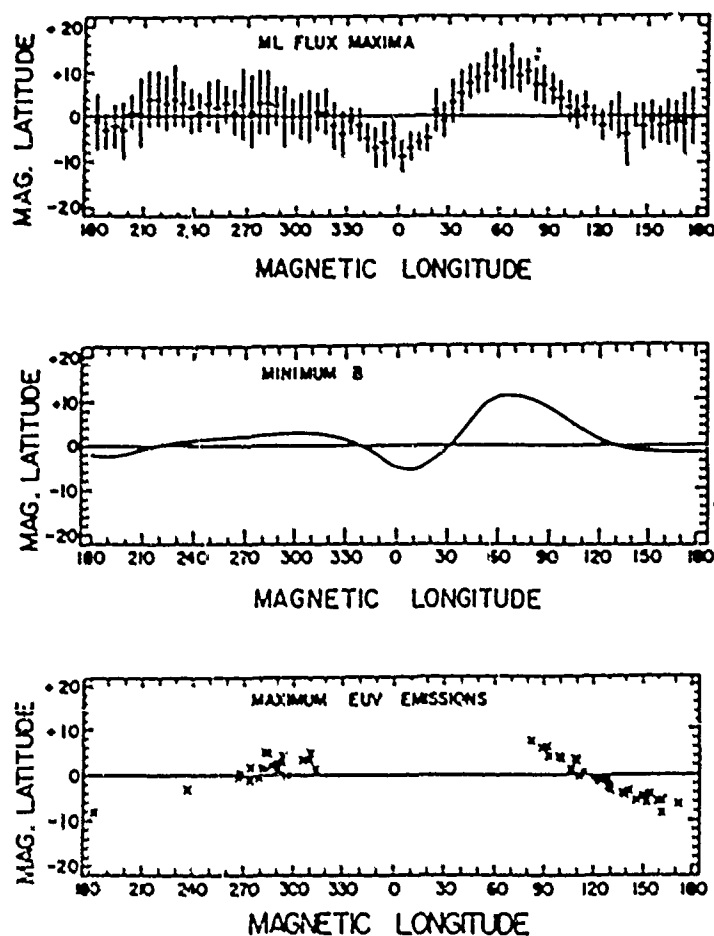


Figure 23. Global distribution of low energy protons.

To investigate any possible longitude dependence of the flux, satellite passes were grouped in three altitude ranges, ( $180 \text{ km} \leq H \leq 215 \text{ km}$ ), ( $225 \text{ km} \leq H \leq 255 \text{ km}$ ), and ( $255 \text{ km} \leq H \leq 285 \text{ km}$ ), based on the altitude at which the measured flux was greatest for each pass. For each range, the passes were binned in  $30^\circ$  longitude intervals and the average rate was computed for each interval. Plots of the average rates for the three altitude ranges are shown in Figure 24 and indicate no statistically significant longitude dependence, as expected from the short proton lifetime at these altitudes.

The orbit of the S81-1 mission varied in altitude over the duration of the mission from  $\sim 180 \text{ km}$  to  $\sim 280 \text{ km}$ . Previous observations reported no apparent altitude variation in the proton intensity from  $\sim 400 \text{ km}$  to  $1000 \text{ km}$ . Over the limited altitude range sampled by the S81-1 mission we have been able to investigate the altitude dependence by binning the dataset into altitude ranges using the satellite altitude at the flux peak as the parameter. All passes falling within a given altitude range were superposed to obtain a mean peak flux, and comparison between different ranges showed a surprisingly large variation. Figure 25 shows

location of the maximum energy deposit in the atmosphere at altitudes of  $130\text{--}160 \text{ km}$  for comparison to airglow observations. He found that for protons of very low energy ( $10\text{--}40 \text{ keV}$ ), the maximum energy deposition occurs  $10\text{--}20^\circ$  off the magnetic dipole equator, which for the actual geomagnetic field corresponds to the minimum B equator. Maximum energy deposition does not necessarily imply maximum particle flux since non-vertical trajectories are important, but the present observations limit such calculations by requiring that the maximum particle flux be confined to the equator down to  $\sim 200 \text{ km}$  altitude. In this regard, the EUV observations of emission from excited  $\text{He}^+$  and  $\text{He}$  (Meier and Weller, 1975) are relevant. The observed spatial distribution of the EUV maxima, shown in Figure 23, agree well with the location of the particle flux maxima. This argues that the ions producing the EUV emission are themselves precipitating, probably from the ring current.



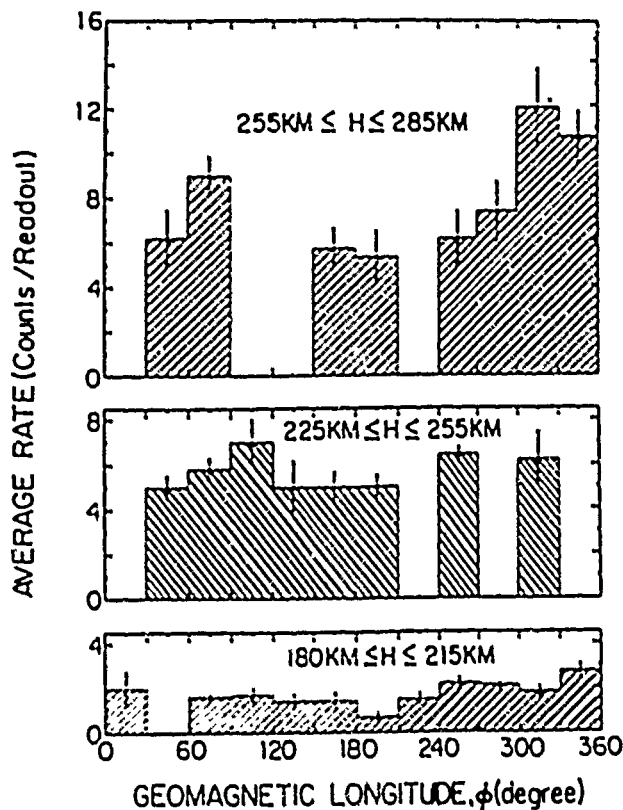


Figure 24. Longitude dependence.

MeV the electron capture cross section is vanishingly small. Thus, in a steady state, the flux of 55 MeV protons is inversely proportional to the atmospheric density, since it is the increasing amount of atmosphere, with decreasing altitude, encountered by the particles that accounts for their loss, probably by ionization energy loss processes.

For the  $\sim 1$  MeV protons, however, the principal source is the neutral hydrogen from charge exchange of protons in the distant magnetosphere, evaluated at the altitude of stripping, times the mean atmospheric density. In the steady state, this flux is expected to be independent of the atmospheric density, as was reported for the high altitude (400-1000 km) observations. The conversion of neutral hydrogen into protons depends upon atmospheric interactions, so that at any altitude, the flux of neutral hydrogen has been reduced by the conversions that have occurred at higher altitudes, and these depend upon the distribution of atmospheric density.

In addition, second order processes must be considered for the  $\sim 1$  MeV protons. There is a "source" contribution from nearby altitudes due to protons at those altitudes which have neutralized and are directed toward the altitude of interest. Furthermore, the exact geometry of the source must be incorporated, and the energy loss during bounce motion along with the cycles of neutralization and restripping must be investigated in detail. Thus, the complete explanation of the observed altitude dependence requires a detailed model of the interplay of these different physical processes.

the Phoenix-1 data compared to the altitude dependence of other measurements found in the literature.

A least squares fit to the Phoenix-1 results shows a power law dependence on altitude,  $H^\beta$ , with exponent  $\beta = 5 \pm 0.5$ . This dependence is essentially the same as that reported for 55 MeV protons observed over the SAA by Filz and Holeman (1965) but is slightly steeper than the newer 55 MeV proton data reported by Parsignault et al. (1981). For very low energies, Goldberg (1974) reports an even steeper altitude dependence. The 55 MeV proton results show the altitude dependence continuing without noticeable change in slope up to  $\sim 700$  km.

The source function for 55 MeV protons is well known since these particles are derived from albedo neutron decay following high energy cosmic ray interactions in the atmosphere. This gives a source that is, to first order, independent of altitude. In addition, at 55

The Phoenix-1 monitor telescope responds to protons over a broad range of energy (0.6 to 9.1 MeV). The spectrum of these protons is expected to be a steeply falling function of energy if the source is indeed the outer radiation belt. The exact energy dependence of the proton flux provides one key test of the model for the origin of these particles. The various observations of the equatorial belt protons are summarized in Figure 26, where we have plotted the peak differential flux versus energy as observed by Moritz (1972), Hovestadt et al. (1972) and Mizera and Blake (1973). The peak differential flux was calculated by dividing

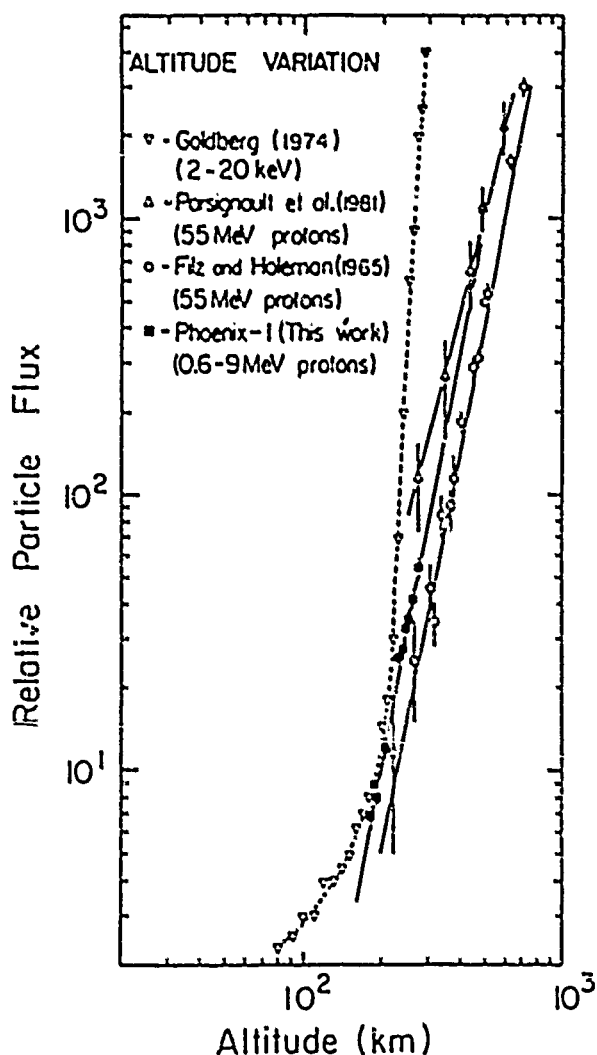


Figure 25. Altitude dependence of particle populations.

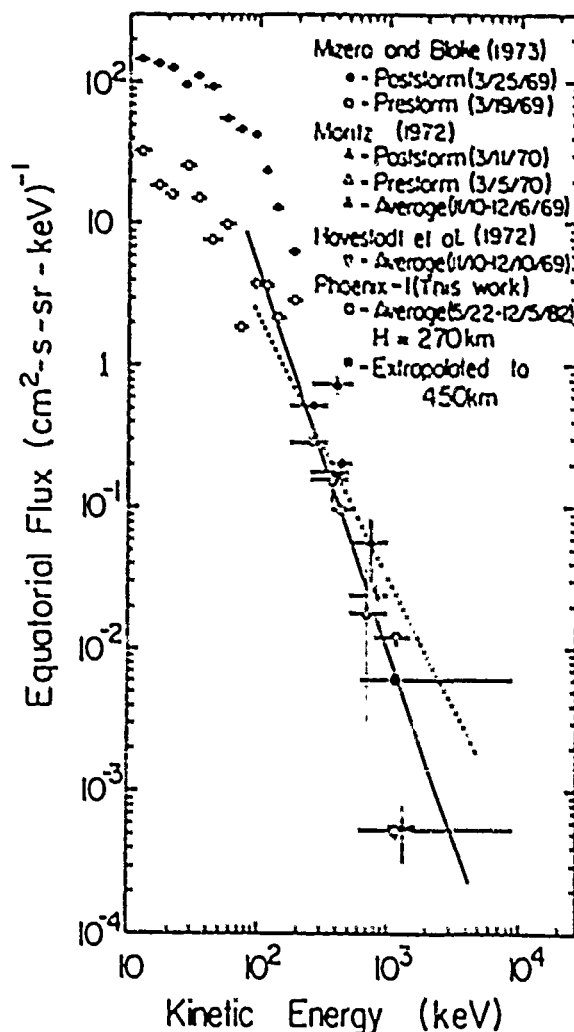


Figure 26. Differential energy spectrum for precipitating protons.

the average peak counting rate by the geometrical factor of the instrument, the readout time, and the energy interval. Both pre-storm, post-storm and average values are presented. At energies above several hundred keV the dependence on geomagnetic conditions lessens, and single day, pre-storm values are equivalent to long period averages, as long as large storms are excluded from the averages. Post-storm conditions show enhanced fluxes up to MeV energies. The Phoenix-1 mission data corresponds for these definitions to average data since no periods following large storms are included in the dataset. Therefore, we have fit a power

energies. The Phoenix-1 mission data corresponds for these definitions to average data since no periods following large storms are included in the dataset. Therefore, we have fit a power law in energy to the previous data above several hundred keV for pre-storm or average conditions, and the result is shown as the solid line characterized by an energy dependence  $E^{-\gamma}$  with exponent  $\gamma = 2.55 \pm 0.11$ . Such a power law may not be the best representation for the energy spectrum. A curve which falls off more steeply at high energy would also give a reasonable fit to the high energy data, but the existing measurements are not sufficient to choose between these possibilities.

For the inferred power law spectrum, the mean energy for ML is  $\sim 1.3$  MeV. For a steeper spectrum at high energy, the mean energy would be reduced. The differential flux is plotted as squares with the full energy interval indicated. The open square represents the measured intensity corresponding to an altitude of  $\sim 270$  km. Using our measured altitude dependence, this result was extrapolated to an altitude of  $\sim 450$  km and is shown as the solid square. This point is considerably above the highest energy point of Moritz (1972). The power law energy spectrum needed to fit the extrapolated ONR-602 observations is shown as the dashed line in the figure and is clearly in disagreement with the previous data. Thus, the flux of precipitating protons at the equator appears to be larger in 1982 than it was during the 1969-1971 time period of the previous observations.

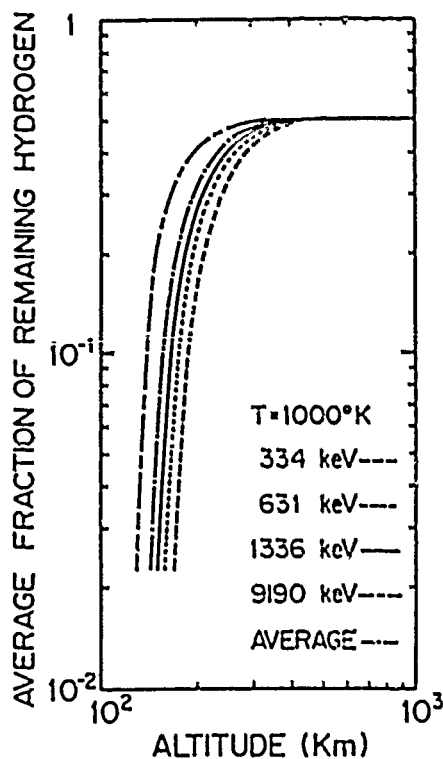


Figure 27. Source Attenuation.

observed by the Phoenix-1 and the EI-92 instruments (Moritz, 1972) in 1982 and 1969-70 respectively (Miah, Mitchell and Wefel, 1989). The absolute flux values were found to be in good agreement for a wide range of values of "q" (for a pitch angle distribution described by  $\sin^q \alpha_E$ , where  $\alpha_E$  is the equatorial pitch angle).

**Source Attenuation Model:** The experimental data presented in the previous subsection shows a strong altitude dependence (180-280 km) in contrast to essentially no altitude dependence observed at higher altitudes (400-1000 km) and a particle flux considerably larger than previous work. Existing models for ring current precipitation cannot explain the ONR-602 results and require modification. Thus, we were led to develop a "new" picture, the Source Attenuation (SA) model (Guzik et al., 1989).

The interpretation of magnetospheric particle data, particularly comparison of observations made by different instruments and/or over different time periods, requires the determination of the absolute intensity of the particles. At a particular altitude and longitude, the trapped particle population is characterized by an equatorial pitch angle distribution to which different instruments may not have the same response. Thus it was first necessary to unfold the effects of the pitch angle distribution from the raw counting rates. We developed a procedure to calculate telescope efficiency as a function of pitch angle and used it to compare the absolute intensities measured for the  $\sim 1$  MeV precipitating protons

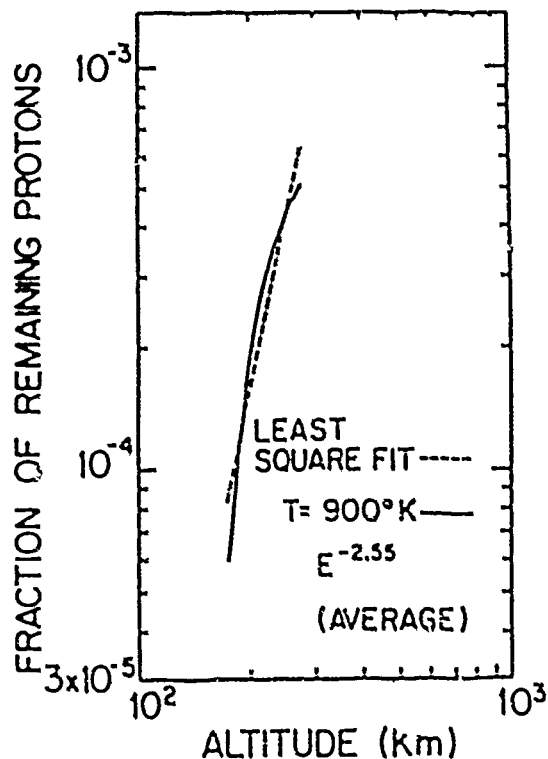


Figure 28. Altitude dependence for Phoenix-1 for SA model.

The SA model assumes the same double charge exchange ring current source as used in previous investigations but incorporates, in addition, all of the loss processes in the atmosphere which have not been treated in detail previously. At large altitudes, the atmospheric column density is so low that there is little attenuation of the neutral hydrogen flux from the source. In this region an altitude independent analysis is a good approximation. At lower altitudes, however, the column density both changes rapidly with altitude and is sufficiently large so that there is a large attenuation. The division between these regions is in the 300-400 km altitude range, just between the regions explored by Phoenix-1 on S81-1 and EI-92 on Azur.

The flux attenuation is illustrated in Figure 27 which shows the calculated attenuation curves, from only charge exchange processes, as a function of altitude for different particle energies. Note the strong altitude dependence at low altitudes. While actually exponential in nature, the curves can be fit by a power law over

the Phoenix-1 altitude range. The cross sections have an energy dependence, leading to the different curves on Figure 27, and this implies that the model calculations must be averaged over the energy spectrum of the observed particles.

Other sources of particle loss must be included. These involve ionization energy loss for the charged protons and pitch angle diffusion into the loss cone. Further, the source geometry, i.e. what fraction of the ring current source that can contribute to the flux at a particular altitude, must also be considered. An analysis of each of these effects has been performed, combined with the attenuation of Figure 27, and averaged over the  $E^{-2.55}$  power law spectrum of Figure 26. The calculated altitude dependence is shown in Figure 28 as the solid line. A power-law fit (dashed line) to the calculations yields an altitude dependence of  $H^{4.6 \pm 0.3}$ , consistent with the measured dependence over the Phoenix-1 altitude interval. With the Phoenix-1 data, it is impossible to observe the small differences between the solid and the dashed curves in Figure 28.

Figure 29 shows the comparison of the absolute flux measured by Phoenix-1 in 1982 (open circles) with that measured by EI-92 in 1969-70 (open squares). The extrapolation of the Phoenix-1 results to the EI-92 altitude via the power law altitude dependence (filled triangles) shows an order-of-magnitude larger flux in 1982, too large a change to be reconciled with a ring current source. The new SA model extrapolation (filled circles), however, shows a flux increase in 1982 by a factor of 1.5-2 depending, weakly, upon the exact value of the

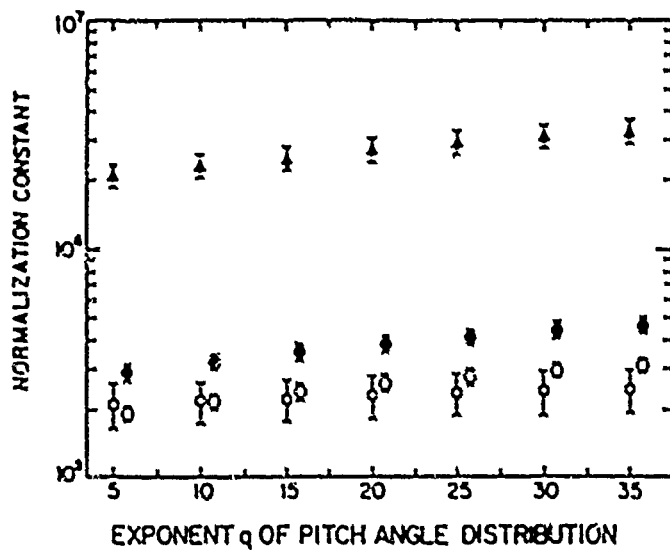


Figure 29. Particle intensity comparison.

the inferred flux depends upon the orientation of the instrument with respect to the magnetic field direction. It has been necessary to develop a detailed procedure to calculate the "efficiency" as a function of particle pitch angle. This procedure is of general enough interest that it was submitted for publication in Nuclear Instruments and Methods in Physics Research. A copy of that paper is attached to describe the calculation for the interested reader.

index of the pitch angle distribution. Thus, there is some evidence for a small, long term temporal variation in this population, due either to an enhanced source, e.g. the ring current, or to differing atmospheric conditions which effect the production and loss of these low energy protons.

Telescope Efficiency: The conclusions of the previous subsection depend upon the comparison of the absolute flux of particles measured by two different telescopes, on different spacecraft, in different epochs. For an isotropic particle distribution, such a comparison is straightforward. For magnetospheric particles, however,

## MAGNETOSPHERIC PARTICLE DETECTION EFFICIENCY OF A CONICAL TELESCOPE

M.A. MIAH

*Department of Mathematical Sciences, University of Arkansas at Pine Bluff, Pine Bluff, Arkansas 71601, USA*

J.W. MITCHELL and J.P. WEFEL

*Department of Physics and Astronomy, Louisiana State University, Baton Rouge, LA 70803, USA*

Received 3 January 1989 and in revised form 17 April 1989

A semi-analytic program has been developed to map the pitch angles of magnetospheric particles onto a detector telescope acceptance cone. The telescope fractional efficiency is defined as the fraction of the pitch angle cone in common with the telescope cone multiplied by the fractional perpendicular component of the exposed detector area, and normalized by  $2\pi$ . Calculations have been performed as a function of the satellite's location, orbital inclination and the zenith angle of the telescope axis, both in dipole and real geomagnetic field models. At the dipole equator, the peak efficiency occurs at  $90^\circ$  pitch angle. In the real geomagnetic field model, the average value of the pitch angle for maximum efficiency is  $\sim 88^\circ$ . The efficiency function depends strongly upon latitude and is independent of longitude in a dipole field, but depends on longitude in the real field model. In either field model, altitude, angle of tilt and orbital inclination have little effect upon efficiency. The efficiency function calculated at the dipole equator can be used at the minimum magnetic field equator with little error, but not for points away from the  $H_{\min}$  position. The results are applied to calculate the absolute flux of magnetospheric particles observed near the equator.

## MAGNETOSPHERIC PARTICLE DETECTION EFFICIENCY OF A CONICAL TELESCOPE

M.A. MIAH

*Department of Mathematical Sciences, University of Arkansas at Pine Bluff, Pine Bluff, Arkansas 71601, USA*

J.W. MITCHELL and J.P. WEFEL

*Department of Physics and Astronomy, Louisiana State University, Baton Rouge, LA 70803, USA*

Received 3 January 1989 and in revised form 17 April 1989

A semianalytic program has been developed to map the pitch angles of magnetospheric particles onto a detector telescope acceptance cone. The telescope fractional efficiency is defined as the fraction of the pitch angle cone in common with the telescope cone multiplied by the fractional perpendicular component of the exposed detector area, and normalized by  $2\pi$ . Calculations have been performed as a function of the satellite's location, orbital inclination and the zenith angle of the telescope axis, both in dipole and real geomagnetic field models. At the dipole equator, the peak efficiency occurs at  $90^\circ$  pitch angle. In the real geomagnetic field model, the average value of the pitch angle for maximum efficiency is  $\sim 88^\circ$ . The efficiency function depends strongly upon latitude and is independent of longitude in a dipole field, but depends on longitude in the real field model. In either field model, altitude, angle of tilt and orbital inclination have little effect upon efficiency. The efficiency function calculated at the dipole equator can be used at the minimum magnetic field equator with little error, but not for points away from the  $H_{\min}$  position. The results are applied to calculate the absolute flux of magnetospheric particles observed near the equator.

## 1. Introduction

Global Geospace Modeling (GEM) is a grand project undertaken by the Solar Terrestrial Research (STR) scientists [4]. The success of GEM partly depends upon our knowledge of (1) loss processes of radiation belt particles at low altitudes and (2) solar-induced and other temporal variability of the quasitrapped particles at low altitude.

GEM covers, as part of the plan, measurements of ions and plasma of all energies. Particle data can be obtained with particle telescopes on board earth-orbiting satellites. Measurement of magnetospheric particle fluxes requires the knowledge of the instrument response function to particles of different pitch angles, since the pitch angle distribution of magnetospheric particles is not isotropic. Facts like the temporal variation of particle flux whose discovery might depend on measurements made by two different instruments also require the calculation of the instrument response function. Thus, the calculation of this fundamentally important quantity is essential in the study of magnetospheric physics.

The observed counting rate of an instrument for a magnetospheric particle population in the pitch angle range  $\alpha_1$  to  $\alpha_2$  and energy range  $E_1$  to  $E_2$  during a readout time interval  $T$  is given by the integral over the incoming particle flux  $j(E, B, L, \alpha, \lambda, \phi, t)$  with the

detector area  $A$  exposed normal to the incident direction, i.e.,

$$R = \frac{1}{T} \int_0^T dt \int_{E_1}^{E_2} dE \int_{\alpha_1}^{\alpha_2} d\alpha \int_A dA \cdot r(\omega) \cdot j(E, B, L, \alpha, \lambda, \phi, t), \quad (1)$$

where  $B$  is the magnetic field,  $L$  is the McIlwain's parameter,  $\alpha$  is the pitch angle,  $\lambda$  is the latitude,  $\phi$  is the longitude, and  $t$  is the time.

We assume the most general expression for flux to be of the form

$$j(E, B, L, \alpha, \lambda, \phi, t) = J_n(B, L, \phi, \lambda, t, q) E^{-h} \sin^q \alpha, \quad (2)$$

where  $J_n$  is the normalization constant, which characterizes the actual particle population,  $\sin^q \alpha$  is the pitch angle distribution and  $E^{-h}$  is the energy spectrum. Then the counting rate can be written as

$$R = J_n(B, L, \lambda, \phi, t, q) \frac{1}{T} \int_0^T dt \int_{E_1}^{E_2} E^{-h} dE \times \int_{\alpha_1}^{\alpha_2} d\alpha \int_{\Omega} d\omega \int_A dA \cdot r(\omega) \sin^q \alpha \quad (3)$$

$$= J_n Q G, \quad (4)$$

where

$$Q = \int_{E_1}^{E_2} E^{-h} dE \quad (5)$$

and

$$G = \int_{\alpha_1}^{\alpha_2} d\alpha \int_{\Omega} d\omega \int_A dA \cdot r(\omega) \sin^2 \alpha = A \mathcal{F}, \quad (6)$$

with

$$\mathcal{F} = \int_{\alpha_1}^{\alpha_2} F(\alpha) f(\alpha) d\alpha, \quad (7)$$

in which  $F(\alpha)$  is the pitch angle distribution function and  $f(\alpha)$  is the efficiency function. The detector count rate is then

$$R = A \mathcal{F} J_n Q \quad (8)$$

whence

$$J_n = \frac{R}{A \mathcal{F} Q}, \quad (9)$$

which is representative of the particle population. Knowledge of the count rate  $R$ , detector area  $A$ , integral of the product of efficiency function and the pitch angle distribution  $\mathcal{F}$ , and the integral spectra  $Q$ , lets us compare  $J_n$  pertaining to different observation times and instruments.

We have calculated the fractional omnidirectional efficiency for a threshold detector telescope of conical shape with shielded surfaces (as shown in fig. 1) on board a three-axis stabilized satellite. The fractional omnidirectional efficiency  $f(\alpha)$  for a particle of a particular pitch angle has been defined as the fraction of the associated space angle intercepted by the telescope cone duly weighted by the perpendicular component of the fractional detector area exposed to the incoming particles, and normalized by the efficiency of a half-omnidirectional detector.

The computer code uses a simple method to find the intercepted portion of the pitch angle cone, instead of

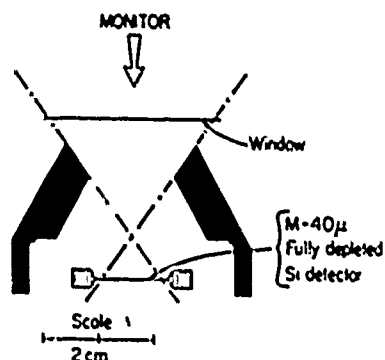


Fig. 1. Geometry of the Monitor telescope used in the efficiency calculation. The full opening angle is  $\beta = 75^\circ$ , the height of the window is  $H = 1.736$  cm. The radius of the circular detector is  $R = 0.5639$  cm, and the radius of the window is 0.776 cm. The shaded shielding stops protons up to  $\sim 40$  MeV.

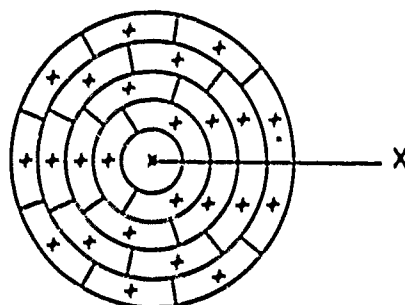


Fig. 2. Division of the radius of the circular detector into five equal parts produces five annular rings (the zeroth order ring is the central disc). Any  $n$ th order ( $n \geq 1$ ) ring is subdivided into  $(2n + 1)$  equal elemental areas, the total number of which is 25. The central point of each of the elemental areas is marked by an "X".

solving the eight-degree equation. Analytical tests have been carried out to verify the results.

## 2. The calculation

In this section an outline of the program is presented. The satellite's location in space is given in geomagnetic coordinates, and a point on the detector surface is described in the detector coordinate system  $X'Y'Z'$ , which has  $O'Z'$  along the telescope axis at zenith angle  $\delta$  (the tilt of the telescope with respect to the local zenith),  $O'X'$  along the anti-flight direction, and  $O'Y'$  chosen to make the system right-handed.

Since the efficiency calculation is relatively easy for a point detector, the whole detector area is represented by a number of points selected in the following way. The given detector area is divided into  $N$  ( $= 10$ ) annular rings (the central one is a disc) by dividing the radius into  $N$  equal divisions. Then,

$$A_n = (2n + 1) \pi \left( \frac{R}{N} \right)^2 \quad (10)$$

is the area of the  $n$ th ring, which is further subdivided into  $(2n + 1)$  equal elemental areas, as shown schematically in fig. 2 for  $N = 5$ . This subdivision leads to  $N \cdot N$  ( $= 100$ ) equal areas whose central points have polar coordinates given by

$$r_n = (2n + 1) \left( \frac{R}{N} \right) \cdot \frac{1}{2}, \quad (11a)$$

$$\gamma_n = \frac{2n' + 1}{2} \frac{360}{2n + 1}, \quad (11b)$$

for the  $n'$ th area in the  $n$ th ring ( $n \geq 1$ ) where  $n' = 0$  and  $2n$ , respectively, for the first and the last areas.

To find the Cartesian components of the unit magnetic field vector in the detector frame situated at the central point of the central ring, we find the components in the geomagnetic coordinate system at the ob-



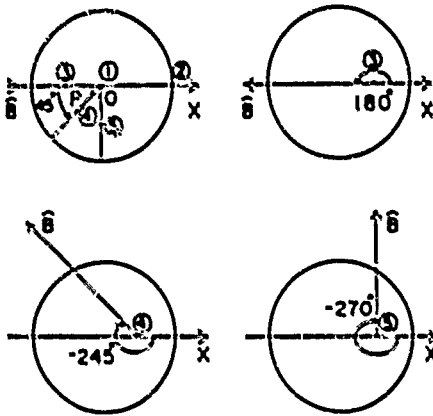


Fig. 3. Illustrations of how the different points on the detector can be reached from the central point. In (a), point (2) can be reached by translation only, whereas points (3), (4) and (5) can be reached by translation through OP and rotations of  $B$  through  $-180^\circ$ ,  $-245^\circ$  and  $-270^\circ$  respectively. Similar descriptions hold for points in (b), (c) and (d).

servation point  $(r, \theta, \phi)$  and apply rotation matrices. Then through translation and rotation of the magnetic field vector, as shown in fig. 3, the representative points at other elemental areas are reached. The cartesian  $B$  vector components become functions of  $\lambda, \phi, \psi, \delta$  and  $\gamma$ , where  $\lambda$  is the colatitude, i.e.  $\lambda = 90^\circ - \theta$ ,  $\phi$  is the longitude and  $\psi$  is the satellite's orbital inclination ( $80^\circ - 120^\circ$  for the polar orbits considered here).

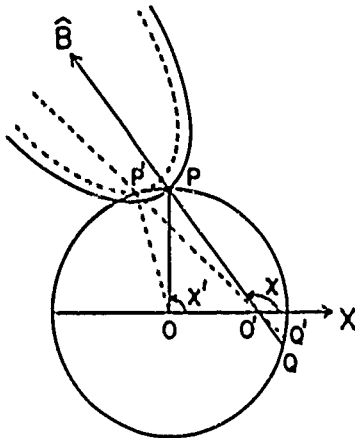


Fig. 4. The circle is the opening ring of the detector.  $O'$  is the projection of the detector point  $(a, 0)$  under consideration. If the telescope cone is right circular,  $QO'P$  is the projection of  $B$ , and the solid conic section is part of the projection of the pitch angle cone opening in the plane of the telescope opening ring. Points P and Q are the contact points for the minimum and the maximum pitch angle cones. If the telescope cone is simply circular, the dotted line and the dotted conic section become the projections, and  $P'$  and  $Q'$  become the contact points.

For a given point at  $(a, 0)$ , the minimum and maximum pitch angles of particles received are found by projecting the  $B$  field and the pitch angle opening ring in the plane of the telescope opening ring, as shown in fig. 4, from which the angle  $\chi$  between  $B$  and the  $X$ -axis is given by:

$$\chi = \cos^{-1} \left( \frac{B_x}{(B_x^2 + B_y^2)^{1/2}} \right). \quad (12)$$

The length of the chord  $O'P$  (or  $O'Q$ ) obtained from the triangle  $PO'O$  (or  $QO'O$ ) is used to determine  $\chi$ . The coordinates of P then define the minimum pitch angle,  $\alpha_{\min}$ , and the coordinates of Q determine the maximum pitch angle,  $\alpha_{\max}$ , both of which are obtained from the following relation:

$$\cos(\alpha(\lambda, \phi, \psi, \delta, \beta, \alpha, H)) = H_x X'' + H_y Y'' + H_z Z'', \quad (13)$$

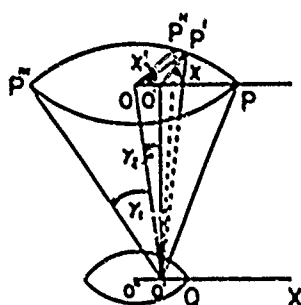
where  $X''$ ,  $Y''$  and  $Z''$  are the components of the unit vector along the incident direction (assumed positive upward). The above geometrical method of determining  $\alpha_{\min}$  and  $\alpha_{\max}$  assumes that both the telescope and the pitch angle cones are right circular. To get the actual contact point  $p'$  between the right circular (axis is perpendicular to the circular base) pitch angle cone and the simply circular (axis is not perpendicular to the circular base) telescope cone,  $\chi'$  corresponding to point p is steadily increased by a fraction of a degree and at each step the pitch angle is evaluated from eq. (13). The pitch angle first increases and then decreases. The  $\chi'$  value at the turning point of the pitch angle gives the correct value of  $\alpha_{\min}$ . The corresponding point of contact for  $\alpha_{\max}$  is  $Q'$ , which is found by steadily decreasing  $\chi'$  until a turning point is found. The quantities  $\alpha_{\min}$  and  $\alpha_{\max}$  are different for different points on the detector. The correct determination of  $\alpha_{\min}$  and  $\alpha_{\max}$  is required to avoid a significant loss in the calculated efficiency.

Any cone of pitch angle  $\alpha_{\min} < \alpha < \alpha_{\max}$  cuts the telescope one at two points. The coordinates of the points of intersection of the pitch angle cone with the telescope cone are obtained by updating  $\chi'$  corresponding to  $\alpha_{\min}$  by adding a telescope geometry dependent step size  $\Delta\chi'$ :

$$\Delta\chi' = \Delta\alpha (H^2 + (R - a)^2)^{1/2} / (R + a) \quad (14)$$

found from fig. 5. The unit vectors  $X''$ ,  $Y''$  and  $Z''$  are calculated, and the pitch angle evaluated. If  $\Delta\alpha = \alpha - \alpha_{\min}$  is not lower than  $0.001^\circ$ , the calculated pitch angle is set equal to  $\alpha_{\min}$ , and the iteration process continues.

After finding the two points of intersection, P and Q, on the opening ring, as illustrated in fig. 6, cross-products of unit vectors directed along OP and OQ are taken with the unit  $B$  vector. The dot product of the resulting



two vectors yields the intercepted portion of the pitch angle cone within the telescope cone.

The efficiency values were calculated in pitch angle steps of  $1^\circ$  in the range between  $\alpha_{\min}$  and  $\alpha_{\max}$ . The cumulative efficiency of all the pitch angles was averaged over the total number of detector points at a given observation point in space.

The calculated efficiency for a given pitch angle represents the fraction of the particle population of that pitch angle received at the given point in space.

Finally, the program is fast. It performs all of the rotations, the search for  $\alpha_{min}$  and  $\alpha_{max}$ , the calculation of cumulative efficiencies and the averaging for the full pitch angle range at all of the 100 detector points in  $\sim 15$  min of CPU time on a VAX 11/750.

### 3. Accuracy of the calculation

To check if the pitch angle range was correctly determined, an alternative method, as shown in fig. 7,

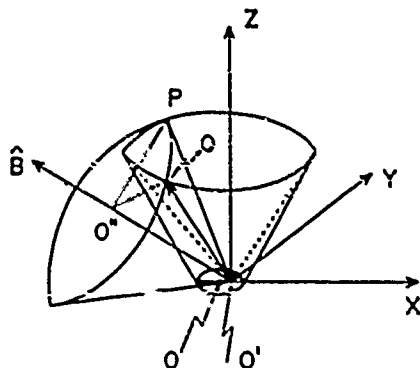


Fig. 6. The point  $O'$  is at  $(a, 0)$  on the detector.  $O'Z$  and  $O'O''$  are the axes of the telescope and the pitch angle cones, respectively.  $P$  and  $Q$  are the points of intersection of the two cones. The part  $O'O''PQ$  of the whole pitch angle cone is intercepted by the telescope cone.

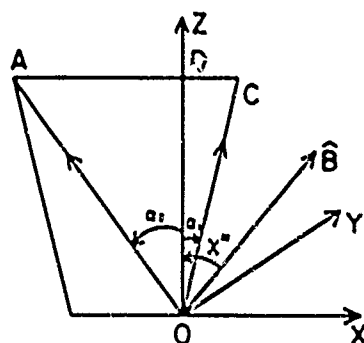


Fig. 7. The section of the telescope cone in the plane of  $\mathcal{N}$  and the OZ-axis which makes two angles with the section boundaries  $= \alpha_1$  (the smaller one and on the side of  $\mathcal{N}$ ) and  $\alpha_2$  (the larger one on the side  $= \mathcal{N}$ ).  $\chi'''$  is the angle between  $\mathcal{N}$  and the OZ-axis. O is a peripheral point on the detector.

was developed. Assuming that the telescope cone is right circular, the maximum and minimum pitch angles are given by:

$$\alpha_{\text{sup}} = X''' - \alpha_1; \quad \alpha_{\text{ms}} = X''' + \alpha_2. \quad (15)$$

The pitch angle ranges calculated by this method and in the computer program are equal. A measure of the precision of finding the coordinates of the points of intersection between the cones at the level of the telescope opening ring is obtained by asking how well the coordinates satisfy the telescope cone equation and the pitch angle cone equation. These are in agreement at a level of  $\sim 10^{-4}$ .

At a representative point on the detector surface it is found that the analytical and the computed values of  $f(\alpha)$  for  $\alpha = 90^\circ$  agree to four decimal places for the configuration  $\chi''' = 90^\circ$ ,  $\lambda = 0^\circ$ ,  $\psi = 90^\circ$  and  $\delta = 0^\circ$ . In addition, an analytic formula for  $f(90^\circ)$  for the whole detector was numerically evaluated using Simpson's method [1]. Also,  $f(90^\circ)$  has been calculated and averaged over 10000 randomly generated points on the detector surface. The analytical, computed and randomly generated values were 0.1167, 0.1228 and 0.1221, respectively, with the program result  $\sim 5\%$  above the numerically integrated result. Further, to check if increasing the number of elemental areas can affect the efficiency function, the detector was divided into 10000 areas and the efficiency function evaluated for particular pitch angles. No significant changes in the efficiency was found.

#### 4. Dependence of $f(\alpha)$ on different parameters

In both the dipole model and a real geomagnetic field model  $f(\alpha)$  has been studied as a function of latitude, longitude, the tilt angle of the telescope axis, the angle of orbital inclination and the direction of

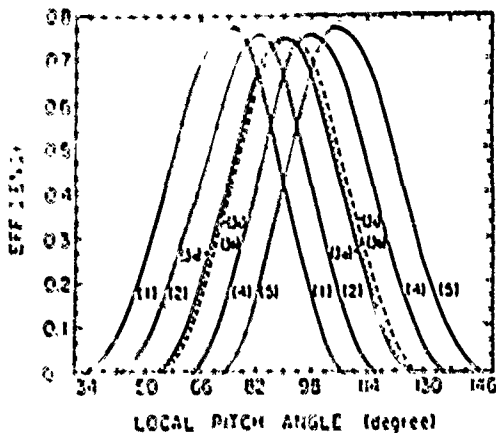


Fig. 8. Latitude and tilt angle variation of efficiency (unnormalized). Curves 1, 2, 3a, 4 and 5 are drawn at  $\lambda = 10^\circ$ ,  $5^\circ$ ,  $0^\circ$ ,  $-5^\circ$ ,  $-10^\circ$ , respectively, for  $\psi = 90^\circ$  and  $\delta = 2.35^\circ$ ,  $\delta = 2.35^\circ$  and  $\psi = 110^\circ$  for curve 3b;  $\delta = 5.0^\circ$  and  $\psi = 110^\circ$  for curve 3c.

flight. In the dipole field model the variation of  $f(\alpha)$  with latitude and tilt angle of the telescope is illustrated in fig. 8. The notable points are the occurrence of the peak efficiency at  $\alpha = 90^\circ$  for  $\lambda = 0^\circ$  and  $\psi = 90^\circ$ , a shift in the peak pitch angle by  $\sim 9^\circ$  for each  $5^\circ$  shift in latitude (as a result of the change in  $\chi'''$ ), and the asymmetric nature of the efficiency curves away from  $\lambda = 0^\circ$ . The effect of the telescope tilt is to displace the curve to the right by  $\sim 1^\circ$  in pitch angle per  $\sim 3^\circ$  in the tilt angle. It is through  $\delta$  that  $f(\alpha)$  depends upon  $\psi$ . For  $\delta = 2.35^\circ$ , if  $\psi$  is changed from  $80^\circ$  to  $120^\circ$  the

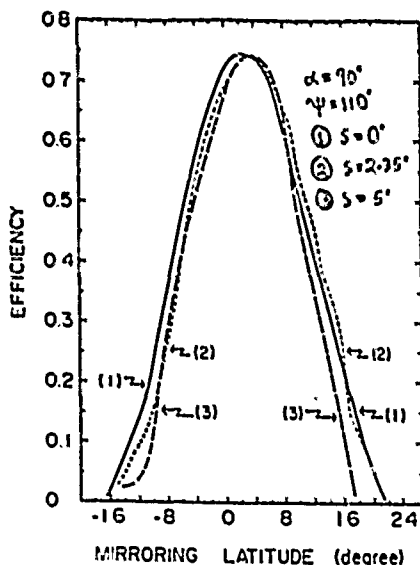


Fig. 9. Variation of efficiency (unnormalized) for mirroring particles with the angle of tilt. All of the curves have the same  $\psi = 110^\circ$ . The curves shift to the right with increasing  $\delta$ .

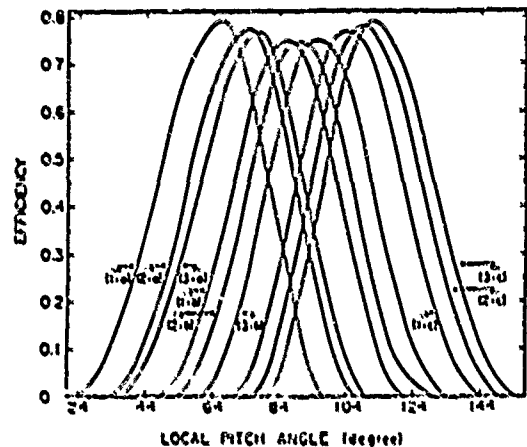


Fig. 10. Variation of efficiency (unnormalized) function in the real field as a function of latitude and longitude. b-curves are at latitudes of the minimum  $B$  equator, a-curves are  $-10^\circ$ , and c-curves are  $+10^\circ$  away from the latitudes of minimum  $B$ . Curves (1a, 1b, 1c) are at  $\phi = 102^\circ$ , (2a, 2b, 2c) are at  $\phi = 270^\circ$ , and (3a, 3b, 3c) are at  $\phi = 230^\circ$ .  $\delta = 2.35^\circ$  and  $\psi = 90^\circ$  for all curves.

efficiency curves move by  $1.6^\circ$ , which is the same as the change in  $\chi'''$ . Fig. 9 shows the efficiency variation for mirroring particles, as a function of the angle of tilt. The displacement of the curves with increasing  $\delta$  are explained by changes in  $\chi'''$ .

In a real field model (IGRF75 extended to 1982),  $f(\alpha)$  was calculated at  $10^\circ$  intervals in geomagnetic longitude along the line of minimum magnetic field strength [5]. On the average, the peak efficiency occurs at  $\alpha \sim 88^\circ$ . This small uncertainty allows us to use the dipole equator  $f(\alpha)$  for the  $B_{\min}$  equator.

Unlike the dipole field, however, the real field makes  $f(\alpha)$  a function of longitude, as shown in fig. 10. Neither the efficiency function evaluated at equal intervals on either side of the  $B_{\min}$  equator and at the same longitude, nor the efficiency function evaluated at the same interval on the same side of the  $B_{\min}$  equator and at different longitudes, are in agreement. The efficiency varies by 5% to 30% within  $\pm 10^\circ$  in latitude from the minimum  $B$  latitudes. Thus, at off- $B_{\min}$  points in the real field the efficiency function deviates from the values at equivalent points in the dipole field. Further, the dependence of  $f(\alpha)$  on orbital inclination and on the tilt angle of the telescope axis is similar to that found for the dipole field. Finally,  $f(\alpha)$  varies little with altitude (over a 500 km altitude change, the efficiency curve shifts by a maximum of  $\sim 2^\circ$  in pitch angle).

## 5. Application of the efficiency function

The efficiency function has been evaluated, in addition, for a detector on AZUR, a magnetically aligned

satellite [3]. We have used this efficiency function to compare the absolute fluxes of magnetospheric protons precipitated at low altitudes along the line of minimum magnetic field strength during two epochs: 1969–70 [3] and 1982 (the telescope of fig. 1). The absolute flux calculation shows that there was 3–10 times more precipitation in 1982 [2].

## 6. Discussion and conclusion

In the calculation, we have defined the pitch angle with respect to the field line passing through the observation point in space, whereas the guiding field line for the particles lies approximately one gyroradius away at different latitude, longitude and altitude. However, for low energy particles, viz., protons of  $\sim 1$  MeV, the gyroradius ( $\sim 5$  km) is relatively small, and the latitude and longitude of the guiding field line are only a few hundredths of a degree away from the observation point. The field line direction does not change significantly over this short distance. In addition, the requirement that the particle trajectory is straight inside the telescope cone is satisfied because of the small dimensions of the telescope compared to the gyroradius. Changes in the efficiency with  $\lambda$ ,  $\phi$ ,  $\delta$ , or  $\psi$  can be easily explained by the change in  $\chi'''$  which controls the limits of applicability of the treatment presented here. If  $\chi'''$  is less than  $\alpha_1$ , particles with  $\alpha = 0^\circ$  can enter the detector (fig. 7). In that case, the efficiency in the pitch angle range  $0^\circ$  to  $\alpha_1$  is 100%. In our instrument, the minimum value of  $\alpha$  is  $\sim 7^\circ$  and the treatment given above can be safely used beyond  $30^\circ$  latitudes where  $\chi'''$  is  $\sim 42^\circ$ .

The comparative study of the behavior of the ef-

iciency function in the two field models suggests the need for evaluation of the efficiency function in the real field, especially for points away from the  $B_{min}$  position, because of the longitude dependence of  $f(\alpha)$ . Altitude variations and small changes in  $\delta$  and  $\psi$  have little effect on  $f(\alpha)$ .

## Acknowledgements

This work was supported at Louisiana State University by ONR under Contract N-00014-83-K-0365. The Monitor telescope used for the efficiency calculation was part of the Phoenix-1 instrument built by the Laboratory for Astrophysics and Space Research at the University of Chicago under Contract NAS 2-24430 and sponsored for spaceflight by ONR.

The authors are thankful to Mrs. Ruth Denny, Mr. Robert Beadle, Miss Stephanie Hicks and others at UAPB's Academic Computer Center for carefully typing and printing the script.

## References

- [1] R.W. Hornbeck, Numerical Methods (Prentice Hall, Englewood Cliffs, NJ, 1975).
- [2] M.A. Miah, J.W. Mitchell, T.G. Guzik and J.P. Wefel, Chapman Conf. on Plasma waves and Instabilities in Magnetospheres and at Comets, Sandai/Mt. Zao, Japan (October, 1987).
- [3] J. Moritz, Z. Geophys. 38 (1972) 701.
- [4] P.H. Reiff, EOE 69 (1988) 786.
- [5] E.G. Stassinopoulos, World Maps of Constant B, L and Flux Contours, NASA SP-3054, Goddard Space Flight Center, Greenbelt, MD (1970).

## VI. BIBLIOGRAPHY

- Adams, J. H., Jr., Silberberg, R. and Tsao, C. H., 1981, NRL Memorandum Report #4506.
- Adams, J. H., Jr. and Partridge, K., 1982, NRL Report.
- Anders, E. and Ebihara, M., 1982, *Geochim. Cosmochim. Acta*, 46, 2363.
- Berko, F. W., Cahill, L. J. Jr. and Fritz, T. A., 1975, *J. G. R.*, 80, 3549.
- Binder, D., Smith, E. C. and Holman, A. B., 1975, *IEEE Trans. Nucl. Sci.*, NS-22, 2675.
- Black, D. C., 1983, *Ap. J.*, 266, 894.
- Blake, J. B., Fennell, J. F. and Hovestadt, D., 1980, *J. G. R.*, 85, 5992.
- Bruckner, G. J., Chater, W. and Kolasinski, W. A., 1980, *IEEE Trans. Nucl. Sci.*, NS-27, 1490.
- Cameron, A. G. W., in "Essays in Nuclear Astrophysics" eds. C.A. Barnes, D. D. Clayton, and D. N. Schramm, (Cambridge, 1982, Cambridge Univ. Press). p. 23.
- Cook, W. R., Stone, E. C. and Vogt, R. E., 1984, *Ap. J.*, 279, 827.
- Dietrich, W. F., and Simpson, J. A., 1979, *Ap. J. Letters*, 231, L91.
- Dietrich, W. F. and Simpson, J. A., 1981, *Ap. J. Letters*, 245, L41.
- Evenson, P., Meyer, P. and Pyle, K. R., 1983, *Ap. J.*, 274, 875.
- Fliz, R. C. and Holeman, E., 1965, *J. G. R.*, 70, 5807.
- Fritz, T. A. and Spjeldvik, W. N., 1981, *Planet. Space Sci.*, 29, 1169.
- Garcia-Munoz, M., Simpson, J. A., Guzik, T. G., Wefel, J. P. and Margolis, S. H., 1987, *Ap. J. Suppl.*, 64, 269.
- Goldberg, R. A., 1974, *J. G. R.*, 77, 5299.
- Guenzer, C. S., Allas, R. G., Campbell, A. B., Kidd, J. M., Petersen, E. L., Seeman, N. and Wolicki, E. A., 1980, *IEEE Trans. Nucl. Sci.*, NS-27, 1485.
- Guzik, T. G., 1988, *Solar Physics*, 118, 185.
- Guzik, T. G., Miah, M. A., Mitchell, J. W. and Wefel, J. P., 1989, *J.G.R.*, 94, 145.
- Hamm, R. N., Turner, J. E., Wright, H. A. and Ritchie, R. H., 1979, *IEEE Trans. Nucl. Sci.*, NS-26, 4892.

- Heikkila, W. J., 1971, J. G. R., 76, 1076.
- Hovestadt, D., Hausler, B. and Scholer, M., 1972, Phys. Rev. Letters, 28, 1340.
- Hovestadt, D., Gloeskler, G., Fan, C. Y., Fisk, L. A., Ipavich, F. M., Klecker, B., O'Gallagher, J. J., and Scholer, M., 1978, Geophys. Res. Lett., 5, 1055.
- Iversen, W. R., 1979, Electronics, (November), p. 44.
- Kolasinski, W. A., Blake, J. B., Anthony, J. K., Price, W. E. and Smith, E. C., 1979, IEEE Trans. Nucl. Sci., NS-26, 5087.
- Konradi, A., 1988, Science, 242, 1284.
- Krassovsky, V. I., Galperin, Yu. I., Jorjio, N. V., Mularchik, T. M. and Boyunova, A. D., in Space Research, ed. P. Muller (Amsterdam, 1964, North Holland Publishing Co.), p. 572.
- Lamport, J. E., Mason, G. M., Perkins, M. A. and Tuzzolino, A. J., 1976, Nucl. Instr. and Methods, 134, 71.
- Lamport, J. E., Perkins, M. A., Tuzzolino, A. J. and Zamow, R., 1980, Nucl. Instr. and Methods, 179, 105.
- Mason, G. M., Gloeckler, G. and Hovestadt, D., 1983, Ap. J., 267, 844.
- Mason, G. M., Reames, D. V., Klecker, B., Hovestadt, D. and von Rosenvinge, T. T., 1986, Ap. J., 303, 849.
- May, T. C. and Woods, M. H., 1979, IEEE Trans. Elect. Dev., ED-26, 2.
- McNulty, P. J., Farrell, G. E., Wyatt, R. C., Rothwell, P. L., Filz, R. C. and Bradford, J. N., 1980, IEEE Trans. Nucl. Sci., NS-27, 1516.
- Meier, R. R. and Weller, C. S., 1975, J. G. R., 80, 2813.
- Mewaldt, R. A., Spalding, J. D., and Stone, E. C., in "Proceedings of the 18th International Cosmic Ray Conference," (Bombay, India, 1983, Tata Institute of Fundamental Research), 4, p. 42.
- Meyer, J. P., 1985, Ap. J. Supplement, 57, 151.
- Miah, M. A., Mitchell, J. W. and Wefel, J. P., 1989, Nucl. Instr. and Methods, A281, 622.
- Mizera, P. F. and Blake, J. B., 1973, J. G. R., 78, 1058.
- Mizera, P. F., Koons, H. C., Schnauss, E. R., Croley, D. R., Jr., Kan, H. K. A., Leung, M. S., Stevens, N. J., Berkopec, F., Staskus, J., Lehn, W. L. and Nanewicz, J. E., 1980, Appl. Phys. Letters, 37, 276.

- Moritz, J., 1972, *Zeitschrift fur Geophysik*, 38, 701.
- Murphy, R. J., Ramaty, R., Forrest, D. J. and Kozlovsky, B., in "Proceedings of the 19th International Cosmic Ray Conference," (LaJolla, CA, 11-23 August, 1985, National Aeronautics and Space Administration, Washington, DC), 4, 249.
- Parsignault, D. R., Holeman, E. and Filz, R. C., 1981, *J. G. R.*, 86, 11439.
- Petersen, E. L., 1980, *IEEE Trans. Nucl. Sci.*, NS-27, 1494.
- Pickel, J. C. and Blandford, J. T., Jr.s 1980, *IEEE Trans. Nucl. Sci.*, NS-27, 1006.
- Prölss, G. W., 1973, *Ann. Geophysics*, 22, (part 4), 503.
- Reames, D. V., 1990, *Ap. J. Suppl.*, (in press).
- Scholer, M., Hovestadt, D. and Gregor, M., 1975, *J. G. R.*, 80, 80.
- Simpson, J. A., in "Annual Review of Nuclear and Particle Science," ed. J. D. Jackson, (Palo Alto, CA, 1983, Annual Reviews, Inc.), 33, p. 323.
- Simpson, J. A., Wefel, J. P. and Zamow, R., in "Proceedings of the 18th International Cosmic Ray Conference," (Bombay, India, 1983, Tata Institute of Fundamental Research), 10, p. 322.
- Simpson, J. A., Munoz, M. G., Perkins, M. and Wefel, J. P., in "CRRES/SPACERAD Experiment Descriptions," eds. M. S. Gussenhoven, E. G. Mullen and R. C. Sagalyn (Air Force Geophysics Laboratory, 1985, Hanscom AFB, MA), p. 163.
- Spjeldvik, W. N. and Fritz, T. A., 1978, *J.G.R.*, 83, 1583.
- Spjeldvik, W. N. and Fritz, T. A., 1981a, *J.G.R.*, 86, 2349.
- Spjeldvik, W. N. and Fritz, T. A., 1981b, *J.G.R.*, 86, 7749.
- Spjeldvik, W. N. and Fritz, T. A., 1981c, *Planet. Space Sci.*, 29, 1227.
- Tinsley, B. A., 1976, *J. G. R.*, 81, 6193.
- Tinsley, B. A., 1979, *J. G. R.*, 84, 1855.
- Van Allen, J. A., Randall, B. A. and Krimigis, S. M., 1970, *J.G.R.*, 75, 6085.
- Voss, H. D., Imhoff, W. L., Mobilia, J. and Gaines, E. E., 1984, XXV COSPAR, Graz, Austria.
- Voss, H. D. and Smith, L. G., 1980, *J. Atmos. Terr. Phys.*, 42, 227.
- Ziegler, J. F. and Lanford, W. A., 1979, *Science*, 206, 776.